ATTENUATION OF SWIRLING MOTION OF A FIRE WHIRL IN A VERTICAL SHAFT

H.Y. Hung[1], Z.M. Gao[2], S.S. Li[2], Y. Gao[2], W.K. Chow[1*] and C.L. Chow[3]

[1]Department of Building Services Engineering, The Hong Kong Polytechnic University, Hong Kong, China

[2]College of Aerospace and Civil Engineering, Harbin Engineering University, Harbin, Heilongjiang, China

[3]Department of Architecture and Civil Engineering, City University of Hong Kong, Hong Kong, China

ORCID ID

W.K. Chow: 0000-0001-8398-3126

C.L. Chow: 0000-0001-5748-4331

Funding

The work described in this paper was supported by a grant from the Research Grants Council of the Hong Kong Special Administrative Region, China for the project "A study of the hazardous consequences of fire whirls generated in a room" (Project No. PolyU 15204918).

[*]Corresponding author:

Fax: (852) 2765 7198; Tel: (852) 2766 5843

Email: wan-ki.chow@polyu.edu.hk

Postal address: Department of Building Services Engineering, The Hong Kong Polytechnic University, Hunghom, Kowloon, Hong Kong.

October 2020

Revised: January 2021

ATTENUATION OF SWIRLING MOTION OF A FIRE WHIRL IN A VERTICAL SHAFT

Experiments on fire whirls generated by a gasoline pool fire in a vertical shaft were carried out. Vortex motions of swirling flame induced by buoyancy above the pool fires were observed to be more vigorous with increase in height. Upward flame motions were resulted due to increase in buoyancy. The phenomenon was described mathematically by solving the vorticity transport equation with reasonable assumptions and appropriate boundary conditions. Analysis gave swirling attenuation along the vertical direction. By measuring heat release rates and fire whirl diameters at different heights, vertical variation of circular speeds of fire whirls was derived.

Key words: Fire whirl, baroclinic force, Buoyancy, Rotating angular velocity, Vertical attenuation

1. Introduction

A fire whirl can be generated under appropriate conditions even inside a building, such as a vertical shaft. Scale models of circulating buoyant plumes were studied by different groups. Scaling studies on fire whirls [1-4] gave large-scale swirling motions to small-scale experimental setup of a few metres tall [5,6]. Klimenko [1] showed that an axisymmetric flow with strong axial vorticity represents a reasonable model for various phenomena of very different scales ranging from the size of a bathtub vortex to the scale of atmospheric cyclones. Lei et al. [5,6] and Kuwana et al. [7,8] had carried out various studies on the relationships of fire whirl height, fuel type, pool diameter, burning rate, and circulation. Recent updates include the behavior of a fire whirl generated by using a burner and examined using Particle Image Velocimetry (PIV) by Hartl and associates [9-11]. Hartl had carried out PIV velocity field study of small-scale pool and burner fire whirl (Fig. 1), which offered new insights into the structure of pool and burner whirls, particularly on the rotating speed near the flame surface and upward motion velocity.

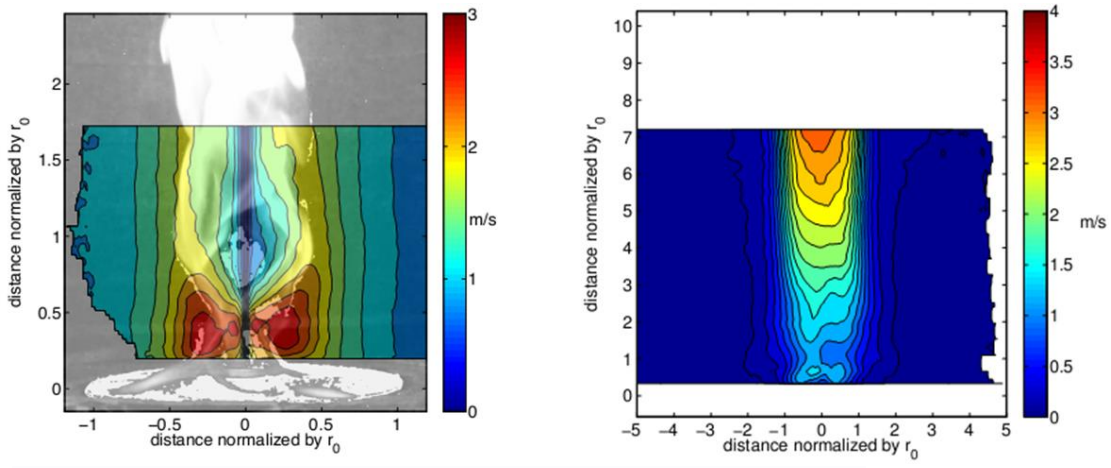

(a) V_θ field (b) V_z field

Fig. 1. Typical data given by Hartl [9]

Fig. 1(a) shows the V_θ fields and Fig. 1(b) shows the V_z fields with typical gap size for the

pool fire reported by Hartl [9]. It was proposed by Lei et al. [5,6] that when upward motion is up to z/H = 0.77 where H is the flame height, maximum centerline velocity is achieved at the end of this region. The plume region extends beyond luminous flame tip to beyond z/H = 1.22. The intermittent region usually occurs at $0.7 \leq z/H < 1.22$, where z/H = 1.22 is to the luminous tip of the fire whirl. In this region, centerline velocity rapidly decreases. As restricted by measuring instruments, small-scale rig was studied [9-11] on the continuous flame region of fire whirls. Measured results by Hartl and Smits [9,10] indicated the centerline axial velocity in the continuous flame region of fire whirls scales as $z^{1/2}$, as the height increases to the plume region, fire whirls behave more like a buoyant plume with a weak swirl, then no swirl. The axial velocity, V_z typically increases first with height before decreasing near the top of the whirl. Measured V_θ fields indicated that near the burning surface, chemical reactions are most vigorous with highest gas temperatures observed, buoyancy and height are related. At position where V_z is small, V_θ is very big. Although the measurements by Hartl were mainly at the continuous flame region of fire whirls $z/H \leq 0.7$, V_θ within this region basically remained unchanged. Beyond z/H = 1:22, V_θ started to decrease to zero at far ends. As stated by Lei et al. [5,6] and Hartl and Smits [9,10], fire whirl height depends mainly on circulation Γ, but not on heat release rates. As a larger scale model was used in this study, particularly with weaker swirling motions, relatively weaker effects of Γ on flame height did not last for a long time. However, effect of heat release rate was stronger.

Emmons and Ying [12] had developed an artificial rotating device. A laboratory-scale experiment was conducted in the 3 m tall device. Acetone fuel pool was used as the source of buoyancy force for the fire. A motorized rotating screen of 2.25 m diameter was used to generate the angular momentum. The rotating screen was driven by an electric motor with a glass window to observe flame motions and shapes. They systematically deduced the effect of angular displacement (Rossby number) and plume buoyancy (Froude number) on the dynamic characteristics of fire whirl. They also pointed out that the turbulence mixing coefficient would decrease with respect to the increase of angular momentum. On the other hand, the coefficient would increase when the flame height increase. Moreover, the burning efficient would increase when the rotation speed is increased. Under a known combustion efficiency of fuel, the burning time is reduced and the flame length is increased by two times. They also proposed a fire plume model based on one-dimensional entrainment theory, but did not propose the pattern of the increment of fire plume height.

Later, Mayle [13] studied the speed and pressure of fire whirl based on the research work by Emmons and Ying. He discovered that plume characteristics is controlled by non-dimensional plume Froude number, Rossby number, second Damkohler number, mixed coefficient and reaction rate. If plume Rossby number is smaller than the Rossby number at the initial stage, the enlargement rate of the plume with respect to height will be greater.

Dimensionless flame height is expressed as a function of dimensionless circulation by Kuwana et al. [8]. When $\Gamma \gg (gL^3)^{1/2}$, the rotational and buoyant velocities are expected to be balanced.

$$\frac{H}{L} \sim \begin{cases} \left(\frac{r^2}{gL^3}\right)^{1/3} & \text{for small pool fires} \\ \frac{r^2}{gL^3} & \text{for large pool fires} \end{cases} \tag{1}$$

and

$$\frac{U_c}{(gL)^{1/2}} \sim Fr_f^{n/2}, n \approx 0.3. \tag{2}$$

The Froude number Fr_f is:

$$Fr_f = \frac{m^2}{\rho_0^2 gL} \tag{3}$$

where m is the mass of fuel consumed per unit burning area per unit time. Also, Π_1 and Π_2 can be regarded as constant.

With the well-established correlation relationship $H/L \sim Fr^n$, where H is the flame height and $1/5<n<1/3$, and L is the horizontal length scale of the burning area.

Simple analysis and simulation were used [8] to verify the validity of applying classical theory in fire whirl scaling. The flame height was found to be proportional to heat release rate and circulation, unrelated to viscosity and turbulent conditions [8]. Flame height of fire whirl was assumed [14] to be dependent on the fuel burning rate which in turn was dependent on the burning temperature, vortex core diameter and flame shape. Differences between rotational flow and irrotational flow were presented. The thermal radiation of rotational flame was stronger. A possible mechanism on why fire whirling resulted in higher flame height was proposed. One reason was heat feedback to the fuel surface, thus enhancing fuel vaporization. Another reason was the interaction of swirling flow and flame. The increase in heat radiation caused by flame circulation made more air being pulled into the flame for combustion. Fire whirl in a semi-enclosed room with vent was studied by Snegirev et al. [15]. Experimental observations indicated that there are periodic creation and annihilation of fire whirl. Temporal averages of burning rate of fuel increased. Vortex motion would affect flame radius and angular velocity of the fire whirl. Swirling would generate a flame shape to emit lower thermal radiation to the pool surface. The air entrainment rate lowered as the swirling motion increased. Numerical simulation by the software Fire3D gave similar predictions to experimental observations. All these suggested that the generation of fire whirl is a very complicated process.

For fire whirls with weak swirling, the flame height depends on [7] fuel combustion characteristics such as fuel pool diameter, fuel type and burning rate, but not on hydrodynamic parameters such as circulation Γ. Flame height was found to be dependent on fuel vaporization in another study [16], which is consistent with literature results.

The ratio of fire whirl flame height to ordinary pool fire height was found to be determined by the fuel surface mass vaporization rate [17-19]. The circulation Γ would enhance vaporization because the fuel surface would have stronger heat transfer ability in the presence of whirl.

Scale modeling experiments on fire whirl created by liquid pool fires in a vertical shaft with a single sidewall gap were reported in previous study [20]. It was observed that a fire whirl could be

generated when the gap width lies within a suitable range of values. The experiment was extended to larger scales by a pool fire burning in a vertical shaft of height 15 m in another study [21]. Correlation between the flame height and swirling velocity in the latter study was reported in Ref. [20]. In order to make comparison of the studies [20-22], the main experimental conditions and flame heights are compiled in Table 1. The critical lateral wind velocity that would generate the most intense fire whirl was determined in these studies. The effect of flow circulation on the increase in flame height was discussed in a number of studies [23-26]. All these works are important for fire hazard assessment [27,29] in modern buildings with green architecture, and particularly useful in studying smoke movement and control in atria [29,30].

Table 1: Conditions of three experimental studies and flame height

Conditions	Vertical shaft scale (cm)	$\frac{\text{gap width}}{\text{channel width}}$ = dimensionless gap	Fuel type	Maximum flame height (cm)	Average flame height (cm)	Oil pool diameter (cm)
Chow and Jan (2009) [18]	35×34×145	$\frac{1.8\sim3.0}{35} = 0.05\sim0.1$	Propanol	75-85	35-65	7.0
Chow et al. 2011 [19]	200×200×1500	$\frac{14,28,56}{200} = 0.07,0.14,0.28$	Gasoline	240,380,450	170,210,220	26,36,46
Wu et al. 2013 [20]	200×200×1500	28×15/200 = 0.14×0.075 (dimensionless width* dimensionless height)	Gasoline	400	30	46
This article	210×210×900	$\frac{33\sim42}{210} = 0.16\sim0.20$	Gasoline	300,360,450	185,225,320	20,26,46

Normally, fire whirls have a larger continuous region than pool fires. However, the length of the continuous region depends on the circulation generation strength and the burning facilities on the pool oil or gas burner, and heat release rate of fuel. Swirling induced more air for the rig with two or four symmetric slits, or just only one gap. Experiments by Lei et al. [5,6] were on a rig with four symmetrical slits. Experiments by Hartl and Smits [10] were on a rig with two symmetric slits. There was only a slit in this study, giving weaker air intake mass and rates. This would give lower pressure gradient than the rig with a single silt. This would result in a shorter continuous region, but a longer intermittent region and plume region. In the base of the continuous region, V_θ and V_z fields agree with the measurement by Hartl [9] in Fig. 1(a). There was stronger swirling at the region near to the fuel surface, no upward movement as shown in the fringe photographs, and buoyancy approached zero. This matched better with the 1/2 or 1/3 power dependence of V_z on z.

As the continuous region was relatively shorter in this study, thermocouples were placed to find the flame centre using the temperature measured, getting relatively shorter regions of weakening swirling and flame heights. In experimental observation, dark red flame spectrum of about 3.32 μm wavelength was taken as the reference. This is different from other references on the measured continuous region only, but included part of the intermittent region and the plume region. Hartl [9] extended the studies by Lei et al. [6] on flame heights, comparing the cases of swirling and not swirling. The swirling continuous region height depends on the values of circulation Γ. Using intermittent regions happened at $0.7 \le z/H < 1.22$, where $z/H = 1.22$ matched with luminous flame tip. At regions near to $z/H = 0.7$, V_z reached maximum, gas temperatures at the continuous region did not

increase, about 700ºC to 900ºC. All values are maximum at the region near to z/H＝0.7. At very short intermittent region, gas temperatures decreased to 500ºC to 600ºC quickly. This study took flame temperatures up to 600ºC, giving different flame heights to their studies. Figure 2 shows the variation of V_z with heights in Lei et al. [6]. The continuous region increased linearly with height.

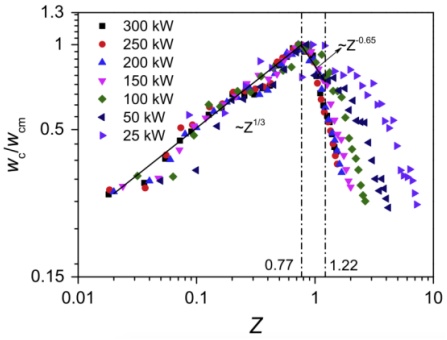

Fig. 2. Typical data given by Lei et al. [6]

The reason is again having only one slit as in the experimental studies [26-31] as referred to in this paper, which is different from others [6-10] in having more symmetrical slits to have stronger air intake rates. Burning was weaker to give shorter continuous regions.

Attenuation of swirling velocity of the fire whirl along the vertical fire axis was studied by including variation in axial velocity and viscous dissipation using the basic equations of vorticity. A similar approach to assessing the same velocity field as in a Burgers vortex was also reported on fire whirl of different scenarios and scales [32]. Momentum implications for buoyant diffusion flames and the formulated rule of vertical movement speed above the fire pool surface by McCaffrey [33] were also employed in the study.

2. Observation from Experiments

Experiments on fire whirl were carried out in open roof vertical shafts of 2.1 m square and height up to 9 m (Fig. 3(a)). Thermocouple trees C and M were located at the centre and corner of the shaft. A gap was opened for supplying air. The gap width was 0.33-0.44 m. Two glass panes of size 2.1 m ×1.5 m were installed on one side for observing the flame characteristics. Three experiments labelled SW-S, SW-M, SW-L represented 0.2 m, 0.26 m and 0.46 m pool fire diameters. The fuel depth was controlled at 4 cm at the beginning to give gasoline volumes of 1.25 litres, 2.12 litres and 6.65 litres respectively.

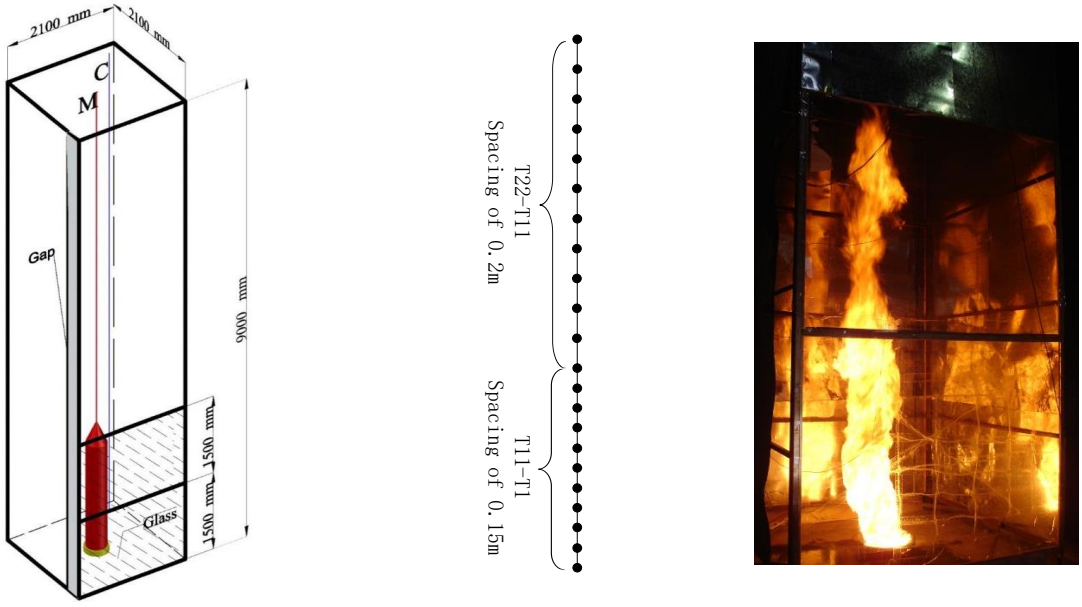

(a) Geometry of shaft

(b) Positions of thermocouples along Tree M and Tree C

(c) Fire whirl moment

Fig. 3. Experimental setup and fire whirl scenario

Fig. 3(b) shows the thermocouple distribution on tree M and C. The temperatures were measured by K type thermocouples and captured by DAQ data acquisition system with a sampling frequency of 10 Hz and Fig. 3(c) is a fire whirl scenario. Bare nickel-chrome and nickel-silicon thermocouples of diameter 0.5 mm and measuring range 0 to 950 ℃ (±1.5 ℃) were used.

Flame height (shown in Fig. 4) is determined from the red flame edge of the video using 3.32 μm wavelength transient flame spectrum conducted by UNI-T UT303D infrared temperature instrument of measuring range -32℃ to 1250℃, or can be detected by thermocouple position which measuring a temperature of 600℃. Photographs were taken at intervals of 1 s. The stable stage average fire whirl height is 1.85 m, 2.25 m and 3.2 m for SW-S, SW-M, SW-L respectively.

As observed from the transient flame heights of the fire whirl in this study, circular motions at the bottom and top were different. For example, air swirled at the bottom, but only moved upward at the upper region. Five zones H1 to H5 above the pool fire can be identified in a typical fire whirl as shown in Fig. 5. The flame movement trajectories at each zone are very different as shown in the figure. The tilted angle to the horizontal of the swirling motion increased from 0° in the lowest zone H1 to 90° in the uppermost zone H5.

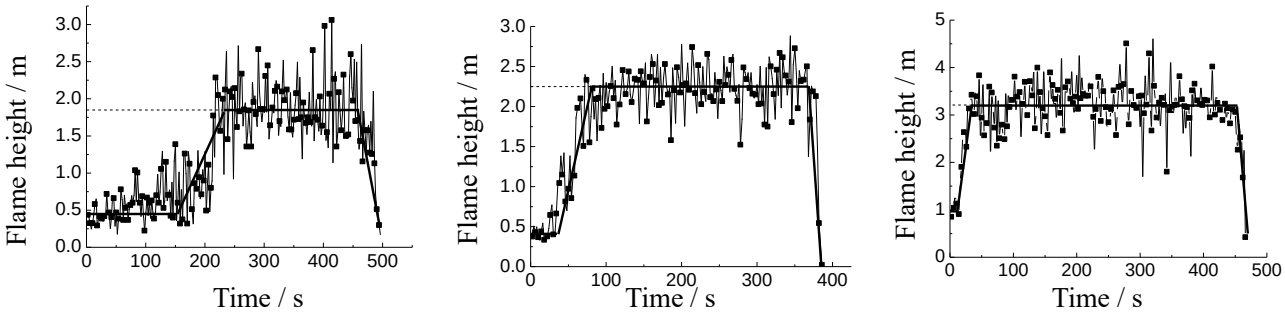

(a) SW-S pool of diameter 0.2 m (b) SW-M pool of diameter 0.26 m (c) SW-L pool of diameter 0.46 m

Fig. 4: Transient flame heights with different pool diameter

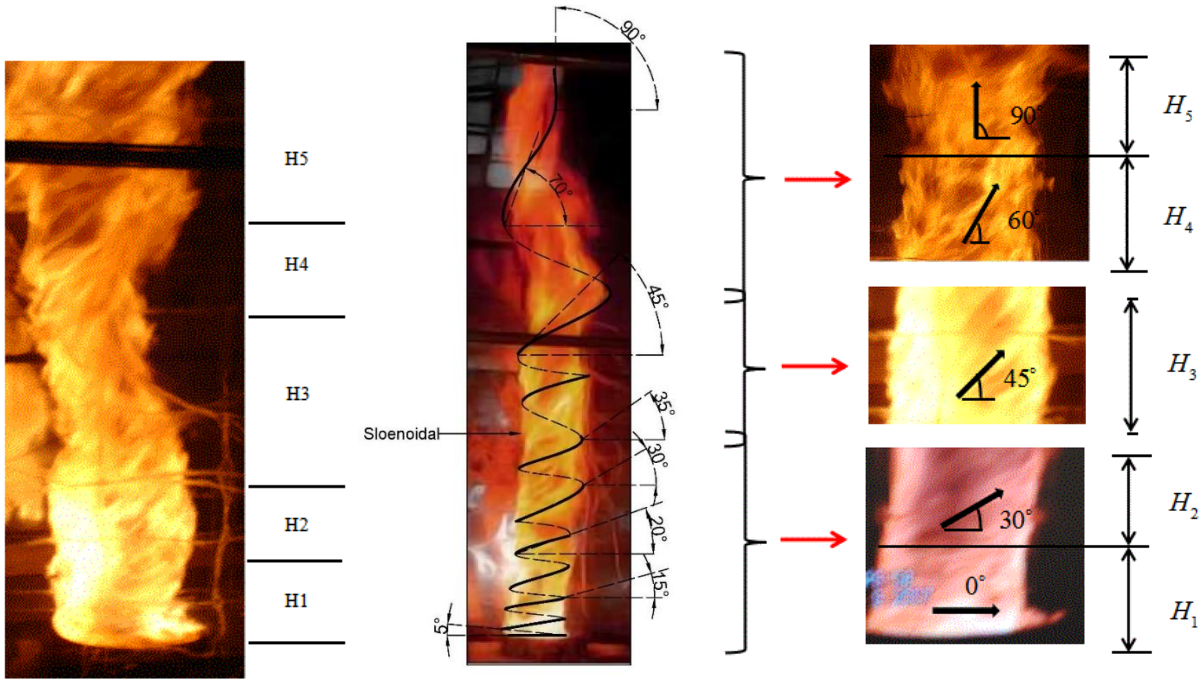

(a) Experimental observation (b) Solenoidal movement (c) Five zones

Fig. 5: Flame trajectories in five zones of a typical fire whirl and schematic diagram of solenoidal movement

The main theme of this paper is to deduce the following using measured flame height (determined by temperature at 600ºC) on V_z :

$$V_z \frac{\partial \omega_z}{\partial z} = \bar{v}_z \frac{\partial^2 \omega_z}{\partial z^2} + \omega_z \frac{\partial V_z}{\partial z} \tag{4}$$

Introducing $\bar{v}_z$ to vary along the *z*-direction with changes in ω_z , giving variation of vorticity Γ along z.

Liquid gasoline pool was used to avoid inducing momentum in using gas fuel burner. There

were no resources to purchase PIV for measuring velocity and better observed circulation. However, soot generated by burning liquid gasoline followed swirling motion, this would give some idea about swirling speed and be able to determine the angle of this motion trajectory tilted to the longitudinal. Observed flame height would also give some hints on analytical study.

Gas movement in zone H5 was vertically upward and in zone H1 it was basically horizontal, as shown in Fig. 5(a). Solenoidal movement was observed in zones H2, H3 and H4, as shown in Fig. 5(b) and Fig. 5(c). All these geometric features of flaming regions are the resultant effects of baroclinic force and buoyancy on swirling motion. A mathematical model is developed in this paper from such experimental observations. Fig. 5 shows the instantaneous video view and photos. In the photo, a part of the carbon black particle trajectory that does not burn completely is visible, and can be seen from different angles of rotation.

A summary of forces driving the gas motion in the five zones is shown in Table 2. Baroclinic force dominates in the lowest zone H1, but buoyancy is the key factor in the uppermost zone H5. Flame features in the zones in between are results of the relative magnitudes of baroclinic force and buoyancy.

It can be seen in Table 2 that baroclinic force is important in zone H1. The temperature difference between inside and outside the flame will be the driving force. When $\nabla\left(\frac{1}{\rho}\right)$ is perpendicular to ∇p, baroclinic force is the maximum. When z increases, zone H2 has $\nabla\left(\frac{1}{\rho}\right)$ and ∇p inclined at an angle of about 60°, baroclinic force is reduced here but buoyancy increases. For zone H3, $\nabla\left(\frac{1}{\rho}\right)$ and ∇p are inclined at 45°, and baroclinic force is very close to buoyancy.

When z increases further (zone H4), the angle between $\nabla\left(\frac{1}{\rho}\right)$ and ∇p is about 30°, and baroclinic force is smaller than buoyancy. When $\nabla\left(\frac{1}{\rho}\right)$ is parallel to ∇p, baroclinic force is zero and the plume is driven solely by buoyancy. In practice, only changes in V_z are considered. For $\nabla\left(\frac{1}{\rho}\right)$ and ∇p inclined at angles from 5° to 85°, it is adequate to study the three zones H2, H3and H4 only. The main driving force for circular motion occurs at the burning surface when the angle between $\nabla\left(\frac{1}{\rho}\right)$ and ∇p is larger than 45°.

Swirling flames result from inclination of contour surfaces of density and pressure. Vortex motion is generated from convection along the tangential direction caused by thermal differences. Baroclinic force would change the directions of fluid motion, and hence generate circular motions. Buoyancy due to density difference would drive fluid to move along the upward directions. Therefore, the relation between the tangential velocity and the vertical velocity of the rotating fluid reflects the relative magnitudes of buoyancy and baroclinic force. For baroclinic force greater than buoyancy, $V_\theta > V_z$ as in zone H2 in Table 2. For baroclinic force of similar magnitude to buoyancy, $V_z \approx V_\theta$ as in zone H3 in Table 2. For baroclinic force smaller than buoyancy, $V_z > V_\theta$ as in H4 region in Table 2.

The Froude number Fr is taken as the ratio of the baroclinic force to buoyancy. Upon generation of a fire whirl, Fr varies from infinity to 0 from the bottom to the top of flame.

The swirling motion of fire whirl was studied analytically using a simple mathematical model in the following sections. Classical models with analytical solutions were applied by focusing on the variations of angular velocity ω_z and tangential velocity V_θ along the radial direction r.

For dimensionless gap width (defined in Table 1) between 0.16 and 0.20, very stable swirling motion is resulted, producing the tallest flame height and highest air temperature under pool diameters of 0.2 m, 0.26 m and 0.46 m. Typical flame pictures in the four stages (initial, ascent, stabilization and declining stage) for the 0.2 m diameter pool fire are shown in Fig. 6.

Table 2: Swirling flow features at different flame heights

Zone	Velocity characteristics	Vertical velocity $\mathbf{V}_z$	Tangential velocity $\mathbf{V}_\theta$	$\mathbf{V}_z / \mathbf{V}_\theta$	Rotational angular velocity ω_z /s^{-1}	Stretching force $\mathbf{F}_c = \boldsymbol{\omega}_z \frac{\partial \mathbf{V}_z}{\partial z}$	Buoyancy force $\mathbf{F}_b = \sigma \mathbf{g}$, $\sigma = \rho - \rho_d$	$\mathbf{F}_c / \mathbf{F}_b$	Baroclinic force $\nabla\left(\frac{1}{\rho}\right) \times \nabla p = \frac{1}{r}\frac{\partial p}{\partial \theta}\frac{\partial}{\partial r}\left(\frac{1}{\rho}\right) - \frac{\partial p}{\partial r}\frac{1}{r}\frac{\partial}{\partial \theta}\left(\frac{1}{\rho}\right)$ $p_1 > p_2 > p_3 > p_4$, $\rho_1 > \rho_2 > \rho_3 > \rho_4$	$\nabla^2 \boldsymbol{\omega} = \nabla^2 \boldsymbol{\omega}_\theta + \nabla^2 \boldsymbol{\omega}_z$ $\tau = \tau_\theta + \tau_z$	Remarks
H5	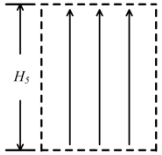	$\mathbf{V}_z = \mathbf{V}_{z\max}$	$\mathbf{V}_\theta = 0$	$\tan 90^\circ = \infty$	$\boldsymbol{\omega}_z = 0$	$\boldsymbol{\omega}_z = 0$, $\frac{\partial \mathbf{V}_z}{\partial z} = 0$	$\sigma \mathbf{g}\left(H_1 + H_2 + H_3 + H_4 + H_5\right)$	$\to 0$	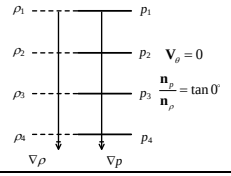	$\nabla^2 \boldsymbol{\omega}_z = 0$, $\nabla^2 \omega_\theta = \tau_{\theta\max}$	Baroclinic force << Buoyancy force $\mathbf{F}_c << \mathbf{F}_b$
H4	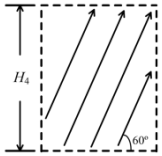	$0 < \mathbf{V}_z < \mathbf{V}_{z\max}$	$0 < \mathbf{V}_\theta$	$\tan 60^\circ = 1.732$	$0 < \boldsymbol{\omega}_z < \boldsymbol{\omega}_{z\max}$	$\boldsymbol{\omega}_z < \boldsymbol{\omega}_{z\max} \frac{\partial \mathbf{V}_z}{\partial z}$	$\sigma \mathbf{g}\left(H_1 + H_2 + H_3 + H_4\right)$	$(0,1)$	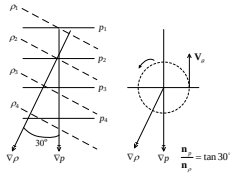	$\tau_\theta > \tau_z$	Baroclinic force < Buoyancy $\mathbf{F}_c < \mathbf{F}_b$
H3	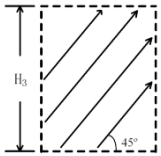	$0 < \mathbf{V}_z$	$0 < \mathbf{V}_\theta$	$\tan 45^\circ = 1$	$0 < \boldsymbol{\omega}_z < \boldsymbol{\omega}_{z\max}$	$\boldsymbol{\omega}_{z\max} \frac{\partial \mathbf{V}_z}{\partial z}$	$\sigma \mathbf{g}\left(H_1 + H_2 + H_3\right)$	1	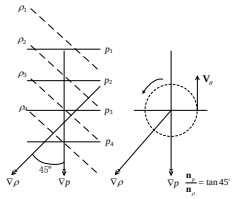	$\tau_\theta \approx \tau_z$	Baroclinic vorticity induced velocity $\mathbf{v}_\theta$ and buoyancy induced velocity $\mathbf{v}_z$ are comparable to the solenoidal component of the velocity
H2	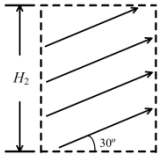	$0 < \mathbf{V}_z < \mathbf{V}_{z\max}$	$0 < \mathbf{V}_\theta < \mathbf{V}_{\theta\max}$	$\tan 30^\circ = 0.577$	$0 < \boldsymbol{\omega}_z < \boldsymbol{\omega}_{z\max}$	$\boldsymbol{\omega}_z < \boldsymbol{\omega}_{z\max} \frac{\partial \mathbf{V}_z}{\partial z}$	$\sigma \mathbf{g}\left(H_1 + H_2\right)$	$(1, +\infty)$	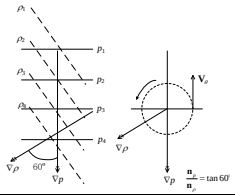	$\tau_\theta < \tau_z$	$\mathbf{F}_c > \mathbf{F}_b$
H1	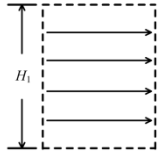	$\mathbf{V}_z = 0$	$\mathbf{V}_\theta = \mathbf{V}_{\theta\max}$	$\tan 0^\circ = 0$	$\boldsymbol{\omega}_z = \boldsymbol{\omega}_{z\max}$	$\boldsymbol{\omega}_{z\max} \frac{\partial \mathbf{V}_z}{\partial z}$	$\sigma \mathbf{g}\left(H_1\right)$ *When* $H_z \to 0$, $\mathbf{F}_b \to 0$	$\to +\infty$	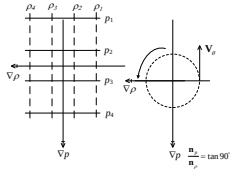	$\nabla^2 \boldsymbol{\omega}_z = \tau_{z\max}$, $\nabla^2 \boldsymbol{\omega}_\theta \approx 0$	Baroclinic *force >> Buoyancy* $\mathbf{F}_c >> \mathbf{F}_b$ *No buoyancy baroclinic vorticity,* $\boldsymbol{\omega}_z$ *would be the largest.*

$0 \le t < 150$ s (a) Initial stage | $150 \le t < 230$ s (b) Ascent stage | $230 \le t < 460$ s (c) Stabilization stage | $230 \le t < 460$ s (d) Declining stage

Fig. 6: Typical flame pictures at four stages of SW-S with 0.2 m diameter pool

3. Analytical Solution for Vorticity and Angular Velocity for a Simplified Equation

The vorticity transport equation can then be written as:

$$\frac{\mathrm{d}\boldsymbol{\omega}}{\mathrm{d}t} = (\boldsymbol{\omega}\cdot\nabla)\mathbf{V} - \boldsymbol{\omega}\left(\nabla\cdot\vec{\mathbf{V}}\right) + \nabla\times\mathbf{f} - \nabla\left(\frac{1}{\rho}\right)\times\nabla p + \nu\nabla^2\boldsymbol{\omega} \tag{5}$$

Suppose the Boussinesq assumption holds, i.e.

$$\sigma = \frac{\rho-\rho_0}{\rho} = \frac{\Delta\rho}{\rho} \tag{5a}$$

$$\rho = \rho_0(1+\sigma) \qquad \sigma << 1 \tag{5b}$$

Assume that the density variation σ is linearly related to temperature T as:

$$\sigma = -\alpha\Delta T \tag{5c}$$

Ideal gas gives the expansion coefficient α as:

$$\alpha = \frac{1}{T} \tag{5d}$$

Putting all equations (5a) to (5d) in (5) gives the incompressible vorticity transport equation:

$$\frac{\mathrm{d}\boldsymbol{\omega}}{\mathrm{d}t} + \mathbf{V}\cdot\nabla\boldsymbol{\omega} = -\nabla\left(\frac{1}{\rho}\right)\times\nabla p + (\boldsymbol{\omega}\cdot\nabla)\mathbf{V} - \nabla\sigma\times\mathbf{g} + \nu\,\nabla^2\boldsymbol{\omega} \tag{6}$$

For incompressible flow, $\nabla\cdot\mathbf{V} = 0$ and $\nabla\cdot\boldsymbol{\omega} = 0$, and excluding the baroclinic term, equation (6) then becomes:

The vorticity transport equation can be written as:

$$\frac{\partial \boldsymbol{\omega}}{\partial t} + \mathbf{V} \cdot \nabla \boldsymbol{\omega} = \boldsymbol{\omega} \cdot \nabla \mathbf{V} + \overline{\nu_r} \, \nabla^2 \boldsymbol{\omega} \tag{7}$$

Equation (7) is applied to zones H1 to H5 and summarized in Table 2, with the baroclinic term given in greater detail.

Equation (7) is transformed into cylindrical coordinates (r, θ, z), with z being the axis for circular motion, and equation (7) becomes:

Assuming rotation along axis z, ω_θ and ω_r are zero:

$$\frac{\partial \omega_z}{\partial t} + V_r \frac{\partial \omega_z}{\partial r} + \frac{V_\theta}{r} \frac{\partial \omega_z}{\partial \theta} + V_z \frac{\partial \omega_z}{\partial z} = \omega_r \frac{\partial (V_z)}{\partial r} + \frac{\omega_\theta}{r} \frac{\partial (V_z)}{\partial \theta} + \omega_z \frac{\partial (V_z)}{\partial z} + \overline{\nu_r} \left(\frac{1}{r} \frac{\partial}{\partial r} \left(r \frac{\partial \omega_z}{\partial r} \right) + \frac{1}{r^2} \frac{\partial^2 \omega_z}{\partial \theta^2} + \frac{\partial^2 \omega_z}{\partial z^2} \right) \tag{8}$$

Assuming ω_z does not vary with θ, then

$$\frac{\partial \omega_z}{\partial t} + V_r \frac{\partial \omega_z}{\partial r} + V_z \frac{\partial \omega_z}{\partial z} = \overline{\nu_r} \left(\frac{1}{r} \frac{\partial}{\partial r} \left(r \frac{\partial \omega_z}{\partial r} \right) + \frac{\partial^2 \omega_z}{\partial z^2} \right) + \omega_z \frac{\partial V_z}{\partial z} \tag{9a}$$

Assuming $V_z = \alpha z + b$

$$\frac{\partial \omega_z}{\partial t} + V_r \frac{\partial \omega_z}{\partial r} + V_z \frac{\partial \omega_z}{\partial z} = \omega_z \alpha + \overline{\nu_r} \left(\frac{1}{r} \frac{\partial}{\partial r} \left(r \frac{\partial \omega_z}{\partial r} \right) + \frac{\partial^2 \omega_z}{\partial z^2} \right) \tag{9b}$$

Flame swirling at steady state can be separated into the parts $\omega_{zr}(r)$ and $\omega_{zz}(z)$ along the r- and z- directions, i.e.,

$$\omega_z (r, z) = \omega_{zr} (r) \omega_{zz} (z) \tag{10}$$

The separation of variables method is one of the common methods to solve the definite solution of linear partial differential equations. The basic idea is to convert the function of several variables into unit function and the partial differential equation into ordinary differential equation. The method of separation of variables was applied to solve the differential equations with the boundary condition satisfied first. Then, the linear combination of these solutions is made by the superposition principle, and finally the superposition coefficient is determined by the remaining definite solution conditions.

Assuming $\omega_{zr}(r)$ and $\omega_{zz}(z)$ are not affecting each other, equation (9) becomes:

$$\frac{\partial \omega_z}{\partial t} = \bar{\nu}_r \frac{1}{r}\frac{\partial}{\partial r}\left(r\frac{\partial \omega_z}{\partial r} \right) + \omega_z \alpha - V_r \frac{\partial \omega_z}{\partial r} \tag{11}$$

$$V_z \frac{\partial \omega_z}{\partial z} = \bar{\nu}_z \frac{\partial^2 \omega_z}{\partial z^2} + \omega_z \frac{\partial V_z}{\partial z} \tag{12}$$

In the above equations, $\bar{\nu}_z$ is the energy attenuation coefficient of ω_z along the *z*-direction, and is much greater than the kinematic viscosity ν. $\bar{\nu}_z$ depends on z and includes minimum attenuated effects due to ω_z and reduction in baroclinic force due to gravity. Combining all experimental observations related to attenuation of circular motion, $\bar{\nu}_z$ is related to h_0. $\bar{\nu}_r$ can be taken as the variation of ω_z attenuation along *r*. Equations (11) and (12) will be solved analytically in this paper. Variation of ω_z along the r-direction and the effects of V_r and $\bar{\nu}_r$ are governed by equation (11), independent of θ and z.

Variation of ω_z under $\bar{\nu}_z$, upward motion V_z, and $\frac{\partial V_z}{\partial z}$ along the z-direction is governed by equation (12). However, this equation cannot be solved analytically because V_z varies along the z-direction with $z^{1/2}$ or $z^{1/3}$. From Fig. 2, ω_z has the highest value at the flame base (z=0). At the top of flame (z=h_0), ω_z is zero. Variation of ω_z is also affected by the average attenuation $\bar{\nu}_z$, not just V_z and $\frac{\partial V_z}{\partial z}$.

For a buoyant flame and a free plume, buoyancy force causes vertical acceleration of the flow inside the flame zone. The stretching term $\omega_z \frac{\partial V_z}{\partial z}$ causes the amplification of non-zero vorticity ω_z. For an upward accelerating flow, $\frac{\partial V_z}{\partial z}$ is positive, giving an increase of ω_z, provided that non-zero background vorticity is introduced. This is the explanation of the development of a rotating core in a rising buoyant flow for positive value of $\frac{\partial V_z}{\partial z}$.

The term $\omega_z \frac{\partial V_z}{\partial z}$ becomes negative in the upper plume where vertical velocity decreases with height. In this region, the vortex tubes are not stretched, but expanded due to decreasing vorticity, since vorticity could be reduced by $\bar{v}_r$ and $\bar{v}_z$. Meanwhile the baroclinic torque and dilatation are also responsible for the reduction.

The axisymmetric flow is considered for which the transport equation for ω_z takes the form (2) with the baroclinic and dilation terms equal to zero. V_z at different z in a buoyant flame and a plume is assumed (this comes from plenty of experimental data, and is basically consistent with the experimental data from Lei et al. [6] in the swirling region (Fig. 2)).

As V_z varied along the z -direction as $z^{1/2}$ or $z^{1/3}$, it is difficult to solve equation (12) analytically. For a pool fire without swirling flame [28], V_z varied with $z^{1/2}$ at the continuous flame region; V_z was almost constant at the intermittent region; and V_z varied with $z^{-1/2}$ at plume region. As observed in experiments generating flame swirling, continuous flame zone is extended and intermittent zone reduced. For small scale fire whirl, $V_z = 6.80z^{1/2}$ was reported by Lei et al. [6] as in Fig. 2. However, equation (12) cannot be solved analytically even when V_z varied with $z^{1/2}$.

Experiments between those with swirling flame by Lei et al. [6] and those without swirling flame by McCaffrey [31] as in Fig. 7 are compared. For regions without flame swirling, vertical variation of V_z in the two sets of experiments are similar. V_z for experiments with swirling flame was higher than those without swirling flame. The proportion of intermittent region in total flame height for swirling flame was smaller. The swirling flame region and plume region have higher portion of flame height. Flame swirling gives higher V_z, and extending to give a longer flaming region. Therefore, the flame height of a fire whirl was extended two to three times that of a non-swirling flame.

Further, the bottom of the flame has the highest swirling speed when a fire whirl is generated as shown in Fig. 5. Lengths of the two zones H1 (with zero V_z but maximum swirling speed), and H5 (with maximum V_z but zero swirling speed), are very short. Therefore, vertical variation of V_z in the five zones observed can be further simplified to three line segments as in Table 3. An example calculation case is shown in Table 4.

Table 3: Results on keeping the first three terms in equation (18) and magnitude of higher-order terms

Test	z / m	C_1	C_2	Δ (%)
Small pool SW-S	0.3	0.973404	0.973402	0.000204
	0.8	0.81235	0.812423	-0.00897
	1.0	0.619307	0.610127	1.482215
Medium pool SW-M	0.3	0.982105	0.982105	5.19×10^{-5}
	0.8	0.87302	0.873031	-0.00136
	1.0	0.767017	0.764775	0.292329
	1.5	0.420601	0.40176	4.479495
Large pool SW-L	0.3	0.991145	0.991145	1.63×10^{-5}
	1.0	0.900666	0.900633	0.003728
	1.5	0.657352	0.641158	2.463494

Table 4: Parameters related to variation of V_z

Tests	Parameters	0 m < z ≤0.49 m	0.49 m < z ≤ 0.94 m	0.94 m < z ≤ 1.27 m
SW-S		4.63	9.07	3.33
	b	0.52	-1.65	3.74
	h_0		1.85 m	
	$\overline{v}_z$	7.92	15.52	5.70
	r_m		0.1 m	
	$\overline{v}_r$	0.0092	0.0181	0.0066
SW-M	Parameters	0 m < z ≤ 0.39 m	0.39 m < z ≤ 0.9 m	0.9 m < z ≤ 1.54 m
	α	4.56	9.37	3.64
	b	0.39	-1.49	3.67
	h_0		2.25 m	
	$\overline{v}_z$	11.54	23.72	9.21
	r_m		0.12 m	
	$\overline{v}_r$	0.0153	0.0315	0.0122
SW-L	Parameters	0 m < z ≤ 0.43 m	0.43 m < z ≤ 1.48 m	1.48 m < z ≤ 2.36 m
	α	2.67	4.42	1.18
	b	0.81	0.06	4.85
	h_0		3.2 m	
	$\overline{v}_z$	13.67	22.63	6.04
	r_m		0.21 m	
	$\overline{v}_r$	0.0281	0.0465	0.0124

Variation of V_z with z for flame above pool fire without swirling can be approximated by linear relations at different heights [33] as shown in Fig. 7. The curve can be approximated by four line segments with slopes α_1 between z_1 and z_2; α_2 between z_2 and z_3; and α_3 between z_3 and z_4 to give analytical solution of equation (12) at different heights as in Fig. 8.

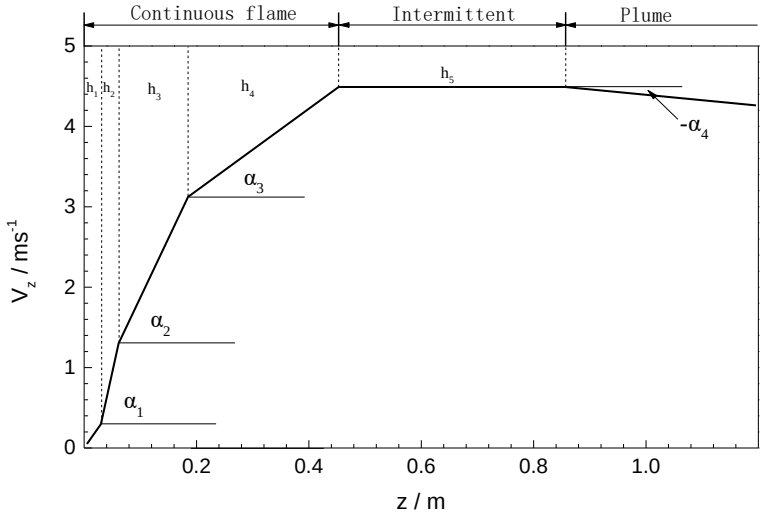

Fig. 7: Linear variation of centerline flame velocity V_z with height z for methanol fire (from McCaffrey 1983 [33])

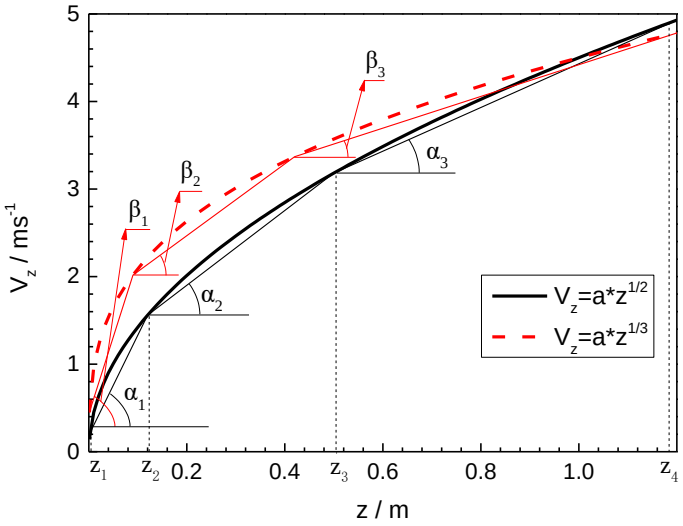

Fig. 8: The 1/2 or 1/3 power dependence of V_z on z with line

Similarly, approximation variation of V_z with z for swirling flame by different line segments of different slopes, equation (12) can be solved. For example, for V_z varied with $z^{1/2}$, three segments of slopes α_1, α_2 and α_3 can be plotted. For V_z varied with $z^{1/3}$, another 3 segments of slopes β_1, β_2 and β_3 are plotted. In this way, equation (9) can be solved.

$$V_z = \alpha z + b \tag{13}$$

Such a complicated swirling problem in fire whirl given by equation (12) cannot be solved easily. In this study, the upward velocities at the flame base with and without swirling are observed to be varying as in Fig. 9. This is indicated in zones H1 and H2 at the bottom of fire whirl (Fig. 5), where the baroclinic effect is the key part and buoyancy effect has little effect. The effect of swirling would give longer flame height due to buoyancy and very small V_z value.

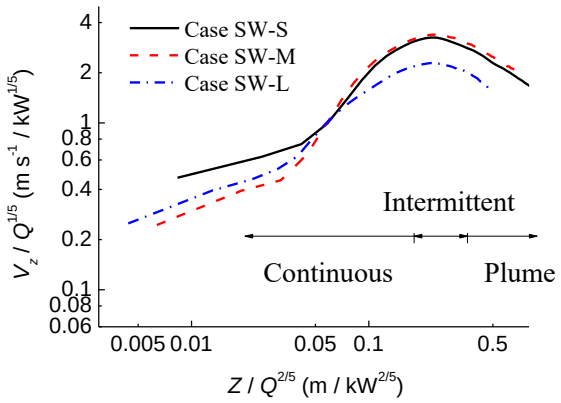

Fig. 9: Variation of vertical velocity with height and heat release rate of fire whirl

As ω_{zr} is a function of r only, equation (11) becomes:

$$\frac{\partial \omega_z}{\partial t}=\frac{\overline{\nu_r}}{r}\frac{\partial}{\partial r}\left(r\frac{\partial \omega_z}{\partial r}\right)+\frac{1}{2}\alpha r\frac{\partial \omega_z}{\partial r}+\alpha\omega_z \tag{14}$$

Following literature [34], substituting γ as α, when α is constant, solution to equation (11) is:

$$\omega_z(r,t)=\frac{\alpha\Gamma_0}{4\pi\left(1-e^{-\alpha t}\right)}\exp\left(-\frac{\alpha r^2}{4\overline{\nu_r}\left(1-e^{-\alpha t}\right)}\right) \tag{15a}$$

When $t\to\infty$,

$$\omega_z(r)=\frac{\alpha\Gamma_0}{4\pi}\exp\left(-\frac{\alpha r^2}{4\overline{\nu_r}}\right) \tag{15b}$$

At r =0, ω_z reaches a maximum value, and $\omega_{zr}(r)$ can be expressed as:

$$\omega_{zr}(r)=\omega_{zr}(r=0)\exp\left(-\frac{\alpha r^2}{4\overline{\nu}_r}\right) \tag{15c}$$

Solving equation (15), by conservation of mass and boundary condition gives limited value V_r at $r=0$.

Substituting $V_z=\alpha z+b$ to equation of mass conservation, and considering boundary condition $r=0$, solution to V_r is:

$$V_r=-\frac{\alpha}{2}r \tag{16}$$

Combining equations (10) and (13) with equation (12) would give a key equation on circular motion:

$$\frac{\mathrm{d}^2\omega_{zz}}{\mathrm{d}z^2}-\left(\frac{\alpha}{\overline{\nu}_z}z+\frac{b}{\overline{\nu}_z}\right)\frac{\mathrm{d}\omega_{zz}}{\mathrm{d}z}+\frac{\alpha}{\overline{\nu}_z}\omega_{zz}=0 \tag{17}$$

Derivation of equation (17) is shown in Appendix 1. Taking the first three terms of the solution of (17) gives:

$$\omega_{zz}(z) \approx \omega_{z\max}\left(1-\frac{1}{2}\frac{\alpha}{\bar{\nu}_z}z^2-\frac{1}{6}\frac{\alpha b}{\bar{\nu}_z^2}z^3-\frac{1}{24}\frac{\alpha^2}{\bar{\nu}_z^2}z^4-\frac{1}{24}\frac{\alpha b^2}{\bar{\nu}_z^3}z^4-\frac{1}{40}\frac{\alpha^2 b}{\bar{\nu}_z^3}z^5-\frac{1}{120}\frac{\alpha b^3}{\bar{\nu}_z^4}z^5 \right.$$
$$\left.-\frac{1}{240}\frac{\alpha^3}{\bar{\nu}_z^3}z^6-\frac{1}{120}\frac{\alpha^2 b^2}{\bar{\nu}_z^4}z^6-\frac{1}{720}\frac{\alpha b^4}{\bar{\nu}_z^5}z^6\right)=C_2\cdot\omega_{z\max} \qquad (18)$$

Results on C_2 of equation (18) for small, medium and large pools are shown in Table 3. Similar results are obtained without keeping the higher-order terms.

Using the boundary conditions $\omega_z(r=0,z=0)$, and let $\omega_{z\max}$ be the maximum value of ω_z, equation (18) gives:

$$\omega_z(r,z) \approx \omega_{z\max}\exp\left(-\frac{\alpha r^2}{4\bar{\nu}_r}\right)\left[1-\frac{\alpha}{2\bar{\nu}_z}z^2-\frac{b\alpha}{6\bar{\nu}_z^2}z^3-\frac{\alpha^2}{24\bar{\nu}_z^2}z^4-\frac{b^2\alpha}{24\bar{\nu}_z^3}z^4\right]=C_1\cdot\omega_{z\max}\exp\left(-\frac{\alpha r^2}{4\bar{\nu}_r}\right) \qquad (19)$$

The expression in equation (19) gives the variation of $\omega_z(r,z)$ along r- and z- directions. $\omega_z(r,z)$ will be affected by attenuation of $\bar{\nu}_r$ and $\bar{\nu}_z$. The values of α and b come from equation (13). Equation (17) has a steady–state solution $\omega_z(r,z)$, which depends on r and z. Results for C_1 are also shown in Table 3.

Putting in $r_{0r}^2 = 4\bar{\nu}_r/\alpha$ and $r_{0z}^2 = 4\bar{\nu}_z/\alpha$, equation (19) can be written as:

$$\omega_z(r,z) \approx \omega_{z\max}\exp\left(-\frac{r^2}{r_{0r}^2}\right)\left[1-2\frac{z^2}{r_{0z}^2}-\frac{2}{3}\frac{b}{\bar{\nu}_z}\frac{z^3}{r_{0z}^2}-\frac{2}{3}\frac{z^4}{r_{0z}^4}-\frac{2b^2}{3\bar{\nu}_z\alpha}\frac{z^4}{r_{0z}^4}\right] \qquad (20)$$

In general,

$$\omega_z=\frac{1}{r}\frac{\partial}{\partial r}(rV_\theta)=\frac{1}{r}\frac{\partial}{\partial r}\left(\frac{\Gamma}{2\pi}\right) \qquad (21)$$

Using the solution from equation (19), the variation of V_θ with z is also deduced.

Solving equation (21) gives:

$$V_\theta \approx \frac{\Gamma_0 r}{2\pi r_{0r}^2}\left(1-\exp\left(\frac{-r^2}{r_{0r}^2}\right)\right)\left[1-2\frac{z^2}{r_{0z}^2}-\frac{2}{3}\frac{b}{\bar{\nu}_z}\frac{z^3}{r_{0z}^2}-\frac{2}{3}\frac{z^4}{r_{0z}^4}-\frac{2b^2}{3\bar{\nu}_z\alpha}\frac{z^4}{r_{0z}^4}\right] \qquad (r\le r_{0r})$$
$$V_\theta \approx \frac{\Gamma_0}{2\pi r}\left(1-\exp\left(\frac{-r^2}{r_{0r}^2}\right)\right)\left[1-2\frac{z^2}{r_{0z}^2}-\frac{2}{3}\frac{b}{\bar{\nu}_z}\frac{z^3}{r_{0z}^2}-\frac{2}{3}\frac{z^4}{r_{0z}^4}-\frac{2b^2}{3\bar{\nu}_z\alpha}\frac{z^4}{r_{0z}^4}\right] \qquad (r\ge r_{0r}) \qquad (22)$$

Equation (22) can be simplified by using the following expression for vorticity Γ:

$$\Gamma \approx \Gamma_0\left(1-\exp\left(-\frac{r^2}{r_{0r}^2}\right)\right)\left[1-2\frac{z^2}{r_{0z}^2}-\frac{2}{3}\frac{b}{\bar{\nu}_z}\frac{z^3}{r_{0z}^2}-\frac{2}{3}\frac{z^4}{r_{0z}^4}-\frac{2b^2}{3\bar{\nu}_z\alpha}\frac{z^4}{r_{0z}^4}\right] \qquad (23)$$

However, Γ still varies with z.

Equation (23) gives the variation of Γ along the z-direction. It is observed that the velocity

along the θ-direction decreases when z increases. On the plane of $z=0$, $r=r_{0r}$:

$$\omega_{z\max}(z=0)=\frac{\Gamma_0}{\pi}\frac{\alpha}{4\bar{\nu}_r}=\left.\frac{\Gamma_0}{\pi r_{0r}^2}\right|_{z=0} \tag{24}$$

Similarly,

$$V_{\theta\max}(z=0)=\left.\frac{\omega_{z\max}r_{0r}^2}{2r}\right|_{r=r_{0r}}=\frac{r_{0r}}{2}\omega_{z\max}=\frac{\Gamma_0}{2\pi}\frac{1}{r_{0r}}=\frac{\Gamma_0}{2\pi}\sqrt{\frac{\alpha}{4\bar{\nu}_r}}=\frac{\Gamma_0}{2\pi}\frac{\sqrt{\frac{\mathrm{d}V_z}{\mathrm{d}z}}}{\sqrt{4\bar{\nu}_r}} \tag{25}$$

The two-dimensional attenuation at the viscous vortex core is similar to Oseen vortex [24,25], the total vorticity being conserved,

$$\Gamma_0=\int_0^\infty 2\pi r\omega_z\mathrm{d}r \tag{26}$$

When r_0 changes with time, the basic motion would be fluid moving from outside to inside, then upward along z with $v=0$ at the symmetric axis $r=0$.

Suppose V_θ reaches the maximum value $V_{\theta\max}$ at radius r_m, where r_m is determined by swirling flame radius.

To obtain the maximum value from the second expression (for $r\geq r_{0r}$) in equation (22),

$$\left.\frac{\mathrm{d}V_\theta}{\mathrm{d}r}\right|_{r=r_m}=0 \tag{27}$$

Solving gives r_m in terms of equivalent radius r_{0r}:

$$r_m\approx 1.1207\sqrt{\frac{4\bar{\nu}_r}{\alpha}}\approx 1.1207r_{0r} \tag{28}$$

Putting equation (28) in the second expression of equation (19),

$$V_{\theta\max}(z,r=r_m)\approx 0.1016\frac{\Gamma_0}{r_{0r}}\left[1-2\frac{z^2}{r_{0z}^2}-\frac{2}{3}\frac{b}{\bar{\nu}_z}\frac{z^3}{r_{0z}^2}-\frac{2}{3}\frac{z^4}{r_{0z}^4}-\frac{2b^2}{3\bar{\nu}_z\alpha}\frac{z^4}{r_{0z}^4}\right] \tag{29}$$

It can be observed from equation (29) that $V_{\theta\max}$ is dissipating along the height z.

Taking r_m as the vortex radius, for regions in the vortex, $r<<1.1207\sqrt{\frac{4\bar{\nu}_r}{\alpha}}$,

$$V_\theta\approx\frac{\alpha\Gamma_0 r}{8\pi\bar{\nu}_r}\left[1-2\frac{z^2}{r_{0z}^2}-\frac{2}{3}\frac{b}{\bar{\nu}_z}\frac{z^3}{r_{0z}^2}-\frac{2}{3}\frac{z^4}{r_{0z}^4}-\frac{2b^2}{3\bar{\nu}_z\alpha}\frac{z^4}{r_{0z}^4}\right] \tag{30}$$

At $z=0$, equation (30) is similar to Rankine vortex [7], where the angular speed $\frac{\alpha\Gamma_0}{8\pi\bar{\nu}_r}$ is taken

as rigid body revolution. For $r >> 1.1207\sqrt{\frac{4\bar{\nu}_r}{\alpha}}$,

$$V_\theta \approx \frac{\Gamma_0}{2\pi r}\left[1-2\frac{z^2}{r_{0z}^2}-\frac{2}{3}\frac{b}{\bar{\nu}_z}\frac{z^3}{r_{0z}^2}-\frac{2}{3}\frac{z^4}{r_{0z}^4}-\frac{2b^2}{3\bar{\nu}_z\alpha}\frac{z^4}{r_{0z}^4}\right] \tag{31}$$

At z=0, equation (28) is also similar to Rankine vortex (viscous vortex distribution of velocity) along the tangential direction.

It is obvious that V_θ decreases along z. Although vorticity is dispersed upward, vortex energy is supplied by motion from outside to inside, compensating the energy lost.

From equation (19),

$$\frac{\omega_z(r,z)}{\omega_{z\max}} \approx \exp\left(-\frac{\alpha r^2}{4\bar{\nu}_r}\right)\left[1-\frac{\alpha}{2\bar{\nu}_z}z^2-\frac{b\alpha}{6\bar{\nu}_z^2}z^3-\frac{\alpha^2}{24\bar{\nu}_z^2}z^4-\frac{b^2\alpha}{24\bar{\nu}_z^3}z^4\right] \tag{32}$$

From equations (22), (25) and (31) gives:

$$\frac{V_\theta}{V_{\theta\max}} \approx \frac{r}{2}\sqrt{\frac{\alpha}{\bar{\nu}_r}}\left(1-\exp\left(\frac{-\alpha r^2}{4\bar{\nu}_r}\right)\right)\left[1-\frac{\alpha}{2}\frac{z^2}{\bar{\nu}_z}-\frac{\alpha^{3/2}}{12}\frac{b}{\bar{\nu}_z^{5/2}}z^3-\frac{\alpha^2}{24}\frac{z^4}{\bar{\nu}_z^2}-\frac{\alpha}{24}\frac{b^2}{\bar{\nu}_z^3}z^4\right] \quad (r \le 2\sqrt{\frac{\bar{\nu}_r}{\alpha}})$$

$$\frac{V_\theta}{V_{\theta\max}} \approx \frac{2}{r}\sqrt{\frac{\bar{\nu}_r}{\alpha}}\left(1-\exp\left(\frac{-\alpha r^2}{4\bar{\nu}_r}\right)\right)\left[1-\frac{\alpha}{2}\frac{z^2}{\bar{\nu}_z}-\frac{\alpha^{3/2}}{12}\frac{b}{\bar{\nu}_z^{5/2}}z^3-\frac{\alpha^2}{24}\frac{z^4}{\bar{\nu}_z^2}-\frac{\alpha}{24}\frac{b^2}{\bar{\nu}_z^3}z^4\right] \quad (r \ge 2\sqrt{\frac{\bar{\nu}_r}{\alpha}}) \tag{33}$$

In approximating $\omega_z(r,z)$ by $\omega_{zr}(r)\cdot\omega_{zz}(z)$, $\omega_{zr}(r)$ and $\omega_{zz}(z)$ are assumed to have no correlation. In practice, ω_z depends on r too, though not too sensitive, particularly at height near z =0. Although the variation of ω_z with z is included and agrees with experimental vorticity characteristics, there are still inadequacies, particularly when the limits $r \to \infty$ and $z \to \infty$, lead to $V_r \to -\infty$, $V_z \to \infty$. Such problems appear in both Burgers and Oseen vortices. Taking V_z as $(\alpha z+b)\left[\exp\left(-\frac{\alpha r^2}{4\bar{\nu}_r}\right)\right]$ would avoid having a divergent solution, but resulting in an equation more difficult to solve.

4. Experimental and Numerical Results for Swirling Flames

Variation of vertical velocity with height above the fuel surface was estimated in the three cases SW-S, SW-M and SW-L, with results plotted in Fig. 9. The vertical velocity was less than 1 ms^{-1} at the flame base, increased with height to a maximum value before dropping to a lower value. The estimated maximum vertical velocities for all three cases were lower than the experimental values. The upper flame part was an intermittent region with flame jumping up and down. Note that the three

curves in Fig. 10 for the three cases are different, with maximum vertical velocity occurring at different times. The rate of rise in vertical velocity and the maximum vertical velocity depended on the heat release rate per unit pool surface area. Higher vertical velocity values were observed for higher heat release rates. As indicated in Fig. 9 and Fig. 10, the maximum vertical velocity was found in the intermittent region below the maximum flame height.

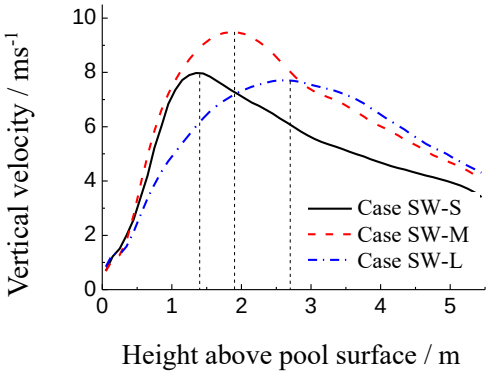

Fig. 10: Variation of vertical velocity with height of fire whirl. Dotted lines indicate the average flame height of fire whirl.

The velocity component V_θ could not be measured accurately. Variation of V_z, maximum flame height h_0 and radius of the swirling flame r_m were estimated from the three cases in Fig. 10 to give the variation of V_z with height z in Fig. 9 by taking heat release rates into account. Variation of vertical velocity with height for a swirling flame is similar to the variation of heat release rate.

It is easy to observe the flame height when a fire whirl is generated. With a simple theory and estimated method, indirect rotating angular velocity can be determined more conveniently than using sophisticated instrument. It is because the angular velocity in the flaming region is difficult to measure.

Variation of the ratio of axial velocity V_z to tangential velocity V_θ with height in a flame surface is plotted in Fig. 11. Based on this ratio, the flaming region can be divided into three zones:

- Zone I : Vigorous swirling flame, $V_z / V_\theta < 0.8$, baroclinic force dominates as in H2 region in Table 1.
- Zone II : Flame transition zone, $0.8 \le V_z / V_\theta < 1.2$, baroclinic force similar to buoyancy as in H3 region in Table 1.
- Zone III : Buoyant flame zone, $V_z / V_\theta \ge 1.2$, buoyancy greater than baroclinic force as in H4 region in Table 1.

Note that the five zones in Fig. 5 show typical movement of flame in the fire whirl. The angles 0°, 30°, 45°, 60°, 90° angles are chosen just for illustrating typical cases.

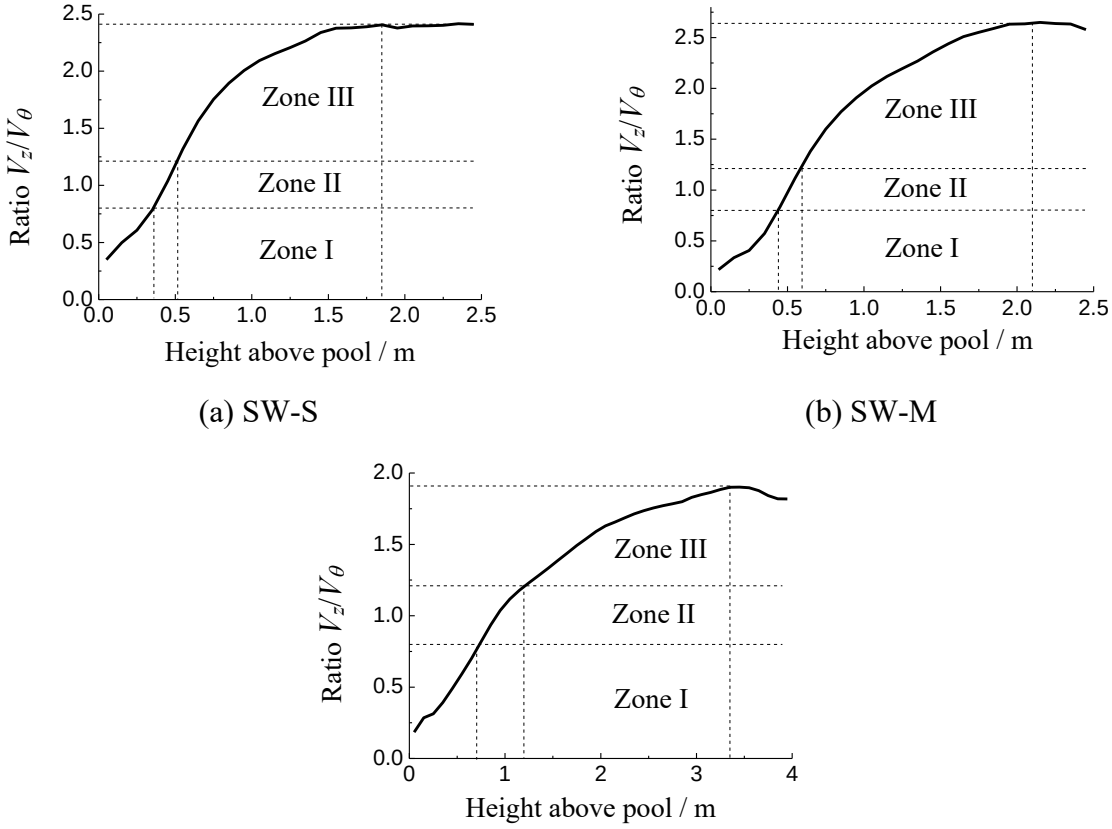

Fig. 11: Variation of the ratio of V_z/V_θ with height

To simplify the analysis for the flame height (taken as h_0), take $\omega_{zz} = 0$ at $z = h_0$. Taking the first two terms on the right-hand side of equation (18),

$$\overline{v}_z \approx \frac{\alpha h_0^2}{2} \tag{36}$$

From equation (25),

$$\overline{v}_r \approx \frac{\alpha r_m^2}{4 \times 1.1207^2} \tag{37}$$

In general, r_m can be taken as the flame swirling radius rather than the pool fire radius.

V_θ reaches the maximum value $V_{\theta \max}$ at the swirling radius r_m as shown in equation (26). Note that $\frac{dV_z}{dz}$ in equation (25) can be determined from experimental data.

5. Empirical Expressions for Pool Fires of Different Size

By dividing the flame into three sections following the above equations, three relations on vertical velocity were deduced from the fire whirl experiments of the three pool fires in Fig. 12:

Small pool (SW-S):

$$\begin{cases} V_z = \alpha_1 z + b_1 = 4.63z + 0.52 & 0\ \text{m} < z \le 0.49\ \text{m} \\ V_z = \alpha_2 z + b_2 = 9.07z - 1.65 & 0.49\ \text{m} < z \le 0.94\ \text{m} \\ V_z = \alpha_3 z + b_3 = 3.33z + 3.74 & 0.94\ \text{m} < z \le 1.27\ \text{m} \end{cases} \quad (38)$$

Medium pool (SW-M):

$$\begin{cases} V_z = \alpha_1 z + b_1 = 4.56z + 0.39 & 0\ \text{m} < z \le 0.39\ \text{m} \\ V_z = \alpha_2 z + b_2 = 9.37z - 1.49 & 0.39\ \text{m} < z \le 0.9\ \text{m} \\ V_z = \alpha_3 z + b_3 = 3.64z + 3.67 & 0.9\ \text{m} < z \le 1.54\ \text{m} \end{cases} \quad (39)$$

Large pool (SW-L):

$$\begin{cases} V_z = \alpha_1 z + b_1 = 2.67z + 0.81 & 0\ \text{m} < z \le 0.43\ \text{m} \\ V_z = \alpha_2 z + b_2 = 4.42z + 0.06 & 0.43\ \text{m} < z \le 1.48\ \text{m} \\ V_z = \alpha_3 z + b_3 = 1.18z + 4.85 & 1.48\ \text{m} < z \le 2.36\ \text{m} \end{cases} \quad (40)$$

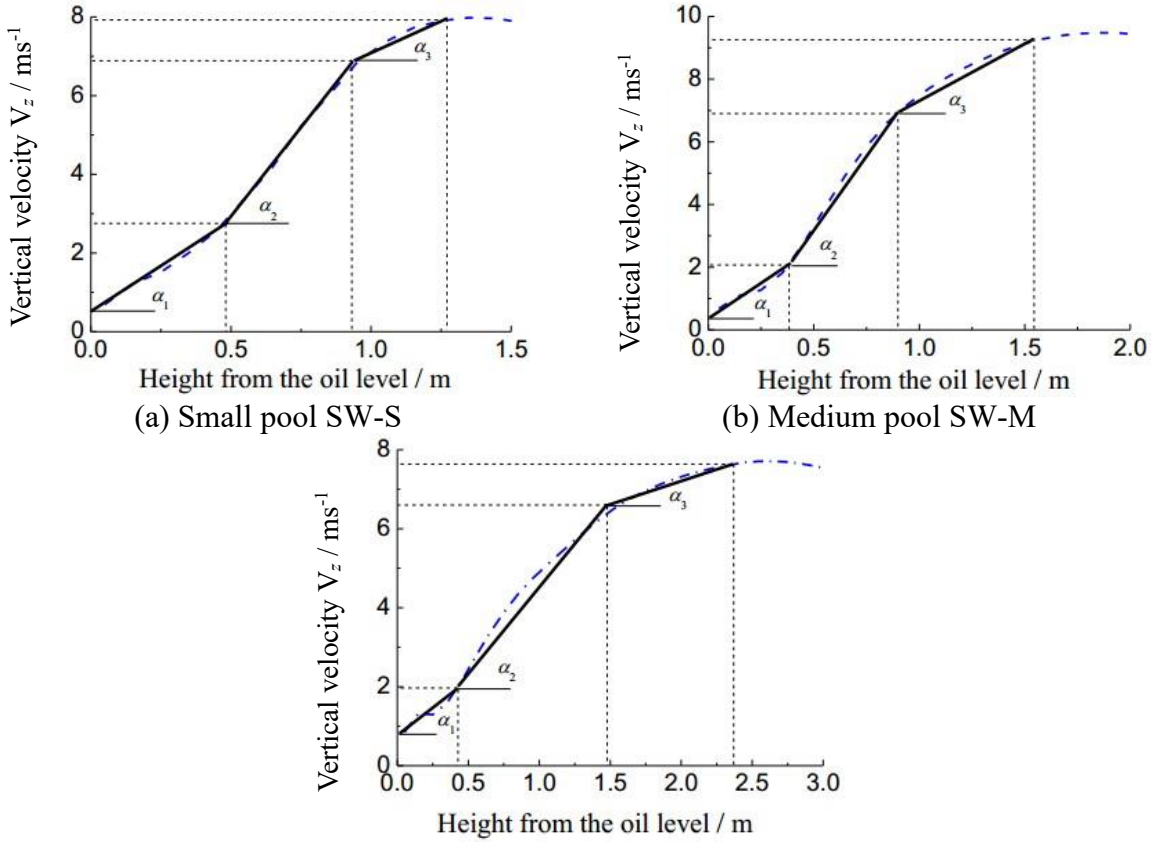

(a) Small pool SW-S

(b) Medium pool SW-M

(c) Large pool SW-L

Fig. 12: Vertical velocity in different sections (The blue dotted line is actually calculated, and the black straight solid line is assumed according to the assumption (38)-(40))

The dotted lines in Fig. 12 come from estimation and experimental correlation in Fig. 11.

In equations (38) to (40), the rotational motions at different heights are assumed to depend on α and b. Five zones are used to describe the properties of swirling motions. Experimental results above suggested that dividing into 5 parts is convenient. When V_z tends to zero, ω_z is approximately maximum at the burning surface, and V_z is maximum far away from the pool surface, with ω_z approaching zero at h_0. Simple examples with only baroclinic force or buoyancy were discussed in many textbooks [24], but both forces are considered in this paper. From the experiments of three pool fire sizes L, M, S, three solutions for $\frac{\partial V_z}{\partial z}$ were obtained for the swirling motion with viscosity $\overline{\nu}_r$ and $\overline{\nu}_z$. Variations of ω_z and V_θ along the z direction are then deduced. All these results are due to the interactions of baroclinic force and buoyancy in the three zones. Ignoring cases with V_z being zero or maximum, knowing the variations of $\frac{\partial V_z}{\partial z}$ in three zones are adequate to solve the equation. Variation of $\frac{\partial V_z}{\partial z}$ can be deduced from Table 4 in this study. Otherwise, $\omega_z \frac{\partial V_z}{\partial z}$ in equation (9) cannot be solved to get the variation of ω_z along z. Equations (17) and (18) are then solved. Analytical solutions obtained previously in the literature were of the Rankine vortex type with the same rotating speed along z. The z change of equations (38)-(40) is limited to the flame length shown in Table 4. This can be applied to tornado, but cannot be applied to strong fire whirl with high temperature difference between high and low levels.

The fire radius r_m for the three experiments SW-S, SW-M and SW-L were 0.1 m, 0.12 m and 0.21 m respectively. Flame heights h_0 were 1.85 m, 2.25 m and 3.2 m as shown in Fig. 4. From equations (38) to (40), and the measured flame height h_0, values of α and b can be deduced. Hence, the values of $\overline{\nu}_r$ and $\overline{\nu}_z$ are estimated and given in Table 4.

More straight lines with different slopes can be used to fit a quadratic curve for the variation of axial velocity with height. In this paper, only three or five straight lines were used for the convenience of simplification to illustrate the approach. Such approximation is simple and feasible as shown in Table 3. Figure 8 shows the approximate results with three straight lines to represent the curve. A better approximation can be obtained by increasing the number of straight lines. However, using three straight lines to represent the curve would be good enough to illustrate the approach. Figure 7 also shows the distribution of the quadratic curve by using five curves instead of that given by McCaffrey 1983 [33]. The rotational velocity from the bottom to the top of the fire whirl decreased gradually from maximum to zero which included all the energy dissipation of the rotational viscosity, buoyancy, thermal dissipation, etc.

A more detailed explanation on above is shown in Appendix 2.

6. Conclusion

In the present study, variation of swirling characteristics and vertical flame velocity with height for internal fire whirls in vertical shafts were investigated using the vorticity transport equation with experimental data. Semi-empirical expressions were obtained, supplemented with discussions based on the relative effects of baroclinic force and buoyancy force. Such relative effects depend on height

and on the heat release rate from the fire pool. Classical solutions of Rankine, Oseen and Burgers vortex are limited to radial variation of ω_z and V_θ, with ω_z and V_θ not changing along the vertical direction. This paper presents a simple theoretical model of the fire whirl and the decay of rotation speed along the height, and gives some experiments to prove it indirectly in a vertical shaft.

Upon generation of a fire whirl, *Fr* varies from infinity to 0 from the bottom to the top of flame. The fire whirl height is mainly affected by fuel surface temperature, external temperature, and density differences. The temperature and density differences produce a very big baroclinic force to maintain the swirling ability of fire whirl when *Fr* approaches infinity. The longer the baroclinic force is maintained along the height, the taller the flame height of the fire whirl.

Nomenclature

D^*	Flame dimensionless diameter
$\mathbf{f}$	Specific force vector at control volume, [N/kg]
$\mathbf{g}$	Acceleration due to gravity, [m^2/s]
H	Height, [m]
h_0	Flame height, [m]
P	Pressure, [Pa]
p_0	Average pressure, [Pa]
r	Radius, [m]
r_m	Swirling flame radius, [m]
r_0	Equivalent radius, [m]
t	Time, [s]
T	Temperature, [K]
V	Velocity vector, [m/s]
Greek number	
ρ	Density, [kg/m^3]
ρ_0	Ambient density, [kg/m^3]
ν	Viscosity, [Ns/m^2]
Γ	Circulation, [m^2/s]
$\boldsymbol{\omega}$	Angular velocity, [rad/s]
σ	Density difference, [kg/m^3]
∇	Hamiltonian operator
$\bar{\nu}$	Energy attenuation coefficient
Subscript	
r, θ, z	Radial, tangential, axial directions

Declaration of Conflicting Interests

The authors declare that there is no conflict of interest.

References

1. Klimenko A (2014) Strong swirl approximation and intensive vortices in the atmosphere. J Fluid Mech 738:268-298.
2. Klimenko A, Williams F (2013) On the flame length in firewhirls with strong vorticity. Combust Flame 160:335-339.
3. Williams FA (2017) Scaling fire whirls. Keynote lecture, Eighth International Symposium on Scale Modelling (ISSM-8), Portland, Oregon, USA, 12-14 September 2017.
4. Tohidi A, Gollner MJ, Xiao H (2018). Fire whirls, Annu Rev Fluid Mech 50:187-213.
5. Lei J et al (2013) Experimental research on flame revolution and precession of fire whirls. Proc Combust Inst 34:2607-2615.

6. Lei J et al (2015) Temperature, velocity and air entrainment of fire whirl plume: a comprehensive experimental investigation. Combust Flame 162:745-758.
7. Kuwana K et al (2011) The burning rate's effect on the flame length of weak fire whirls. Proc Combust Inst 33:2425-2432.
8. Kuwana K et al (2008) Scaling fire whirls. Fire Saf J 43:252-257.
9. Hartl KA (2016) Experimental investigation of laboratory fire whirls. PhD Thesis, Princeton Univ.
10. Hartl KA, Smits AJ (2016) Scaling of a small scale burner fire whirl. Combust Flame 163:202-208.
11. Wang P, Liu N, Hartl K, Smits A (2016). Measurement of the flow field of fire whirl, Fire Technology, 52(1):263-272.
12. Emmons HW, Ying SJ. The fire whirl (1966). 11th International Combustion Symposium, 475-488.
13. Mayle RE (1970). Aerodynamics of the fire whirl, PhD Thesis, Harvard University, 1-250.
14. Chuah KH, Kushida G (2007) The prediction of flame heights and flame shapes of small fire whirls. Proc Combust Inst 31: 2599-2606.
15. Snegire AY et al (2004) Numerical studies and experimental observations of whirling flames. Int J Heat Mass Transfer 47(12): 2523-2539.
16. Lei J, Liu N (2016) Burning rates of liquid fuels in fire whirls. Combust Flame 159: 2104-2114.
17. Zhou K, Liu N, Yuan X (2016) Effect of wind on fire whirl over a line fire. Fire Technol 52(3): 865-875.
18. Wang P, Liu N, Liu X, Yuan X (2018) Experimental study on flame wander of fire whirl. Fire Technol 54(5): 1369-1381.
19. Zhou KB et al (2013) Effect of flow circulation on combustion dynamics of fire whirl. Proc Combust Inst 34: 2617–2624.
20. Chow WK, Han SS (2009) Experimental investigation on onsetting internal fire whirls in a vertical shaft. J Fire Sci 27(6): 529-543.
21. Chow WK et al (2011) Internal fire whirls in a vertical shaft. J Fire Sci 29(1): 71-92.
22. Wu HM et al (2013) Studies on internal fire whirls in a vertical shaft with a single corner gap. Journal of Applied Fire Science 22(2): 179-200.
23. Tomizuka T et al (2011) The burning rate's effect on the flame length of weak fire whirls. Proc Combust Inst 33(2): 2425-2432.
24. Wada Y, Kuwana K (2011) Influence of vortex structure on fire whirl behavior. Fire Safety Science 10: 671-679.
25. Zou GW et al (2019) A study of correlation between flame height and gap width of an internal fire whirl in a vertical shaft with a single corner gap. Indoor Built Environ 29(1): 34-45.
26. Chow WK et al (2017) Dependence of flame height of internal fire whirl in a vertical shaft on fuel burning rate in pool fire. Appl Therm Eng 121: 712-720.
27. Chow WK (2003) Fire safety in green or sustainable buildings: Application of the fire engineering approach in Hong Kong. Architectural Science Review 46(3): 297-303.
28. Chow WK (2015) Performance-based approach to determining fire safety provisions for buildings in the Asia-Oceania regions. Build Environ 91: 127-137.
29. Chow WK (1995) A comparison of the use of fire zone and field models for simulating atrium

smoke-filling processes. Fire Saf J 25(4): 337-353.
30. Chow WK et al (2009) Numerical studies on atrium smoke movement and control with validation by field tests. Build Environ 44(6): 1150-1155.
31. Hung HY et al (2019) Observation on a fire whirl in a vertical shaft using high-speed camera and associated correlation derived. Thermal Science, DOI:10.2298/tsci181004266h. Published online first May 2019.
32. Saffman PG et al (1992) Vortex Dynamics. Cambridge: Cambridge University Press, p. 253.
33. McCaffrey BJ (1983) Momentum implications for buoyant diffusion flames. Combust Flame 52: 149-167.
34. Wu JZ, Ma HY, Zhou MD (2005), Vorticity and Vortex Dynamics, Springer.

FT_IFWR20-1m

Appendix 1. Derivation of key equation (17)

Equation (17) is given as:

$$\frac{\mathrm{d}^2\omega_{zz}}{\mathrm{d}z^2}-(\frac{\alpha}{\overline{v}_z}z+\frac{b}{\overline{v}_z})\frac{\mathrm{d}\omega_{zz}}{\mathrm{d}z}+\frac{\alpha}{\overline{v}_z}\omega_{zz}=0$$

Let

$$\omega_{zz}=\sum_{n=0}^{\infty}a_n z^n=a_0+\sum_{n=1}^{\infty}a_n z^n \tag{A1}$$

$$\frac{\mathrm{d}\omega_{zz}}{\mathrm{d}z}=\sum_{n=1}^{\infty}na_n z^{n-1} \tag{A2}$$

$$\frac{\mathrm{d}^2\omega_{zz}}{\mathrm{d}z^2}=\sum_{n=2}^{\infty}n(n-1)a_n z^{n-2}=\sum_{n=0}^{\infty}(n+2)(n+1)a_{n+2}z^n=2a_2+\sum_{n=1}^{\infty}(n+2)(n+1)a_{n+2}z^n \tag{A3}$$

Putting into equation (18) gives:

$$2a_2+\sum_{n=1}^{\infty}(n+2)(n+1)a_{n+2}z^n-\frac{\alpha}{\overline{v}_z}z\sum_{n=1}^{\infty}na_n z^{n-1}-\frac{b}{\overline{v}_z}\sum_{n=1}^{\infty}na_n z^{n-1}+\frac{\alpha}{\overline{v}_z}a_0+\frac{\alpha}{\overline{v}_z}\sum_{n=1}^{\infty}a_n z^n=0$$

$$2a_2+\sum_{n=1}^{\infty}(n+2)(n+1)a_{n+2}z^n-\sum_{n=1}^{\infty}\frac{\alpha}{\overline{v}_z}na_n z^n-\frac{b}{\overline{v}_z}a_1-\sum_{n=1}^{\infty}\frac{b}{\overline{v}_z}(n+1)a_{n+1}z^n+\frac{\alpha}{\overline{v}_z}a_0+\sum_{n=1}^{\infty}\frac{\alpha}{\overline{v}_z}a_n z^n=0$$

$$2a_2-\frac{b}{\overline{v}_z}a_1+\frac{\alpha}{\overline{v}_z}a_0+\sum_{n=1}^{\infty}[(n+2)(n+1)a_{n+2}-\frac{b}{\overline{v}_z}(n+1)a_{n+1}-(\frac{\alpha}{\overline{v}_z}n-\frac{\alpha}{\overline{v}_z})a_n]z^n=0$$

$$2a_2-\frac{b}{\overline{v}_z}a_1+\frac{\alpha}{\overline{v}_z}a_0=0 \quad\Rightarrow\quad a_2=-\frac{\alpha}{\overline{v}_z}\frac{a_0}{2}+\frac{b}{\overline{v}_z}\frac{a_1}{2}$$

Or

$$(n+2)(n+1)a_{n+2}-\frac{b}{\overline{v}_z}(n+1)a_{n+1}-(\frac{\alpha}{\overline{v}_z}n-\frac{\alpha}{\overline{v}_z})a_n=0 \qquad (n\geq 1)$$

$$\Rightarrow\quad a_{n+2}=\frac{\alpha}{\overline{v}_z}\frac{n-1}{(n+2)(n+1)}a_n+\frac{b}{\overline{v}_z}\frac{1}{n+2}a_{n+1}$$

Each term a_n has to be known. Putting

$$a_0=a_0,\ \ a_1=0,$$

$$\Rightarrow\ a_2=-\frac{\alpha}{\overline{v}_z}\frac{a_0}{2}$$

$$a_3=\frac{b}{\overline{v}_z}\frac{1}{3}a_2=\frac{b}{\overline{v}_z}\frac{1}{3}(-\frac{\alpha}{\overline{v}_z}\frac{a_0}{2})=-\frac{1}{6}\frac{\alpha b}{\overline{v}_z^2}a_0$$

$$a_4=\frac{\alpha}{\overline{v}_z}\frac{1}{12}a_2+\frac{b}{\overline{v}_z}\frac{1}{4}a_3$$

$$=\frac{\alpha}{\overline{v}_z}\frac{1}{12}\left(-\frac{\alpha}{\overline{v}_z}\frac{a_0}{2}\right)+\frac{b}{\overline{v}_z}\frac{1}{4}\left(-\frac{1}{6}\frac{\alpha b}{\overline{v}_z^2}a_0\right)=-\frac{1}{24}\left(\frac{\alpha}{\overline{v}_z}\right)^2a_0-\frac{1}{24}\frac{\alpha b^2}{\overline{v}_z^3}a_0$$

$$a_5 = \frac{\alpha}{\bar{v}_z}\frac{2}{20}a_3 + \frac{b}{\bar{v}_z}\frac{1}{5}a_4 = \frac{\alpha}{\bar{v}_z}\frac{1}{10}\left(-\frac{1}{6}\frac{\alpha b}{\bar{v}_z^2}a_0\right) + \frac{b}{\bar{v}_z}\frac{1}{5}\left(-\frac{1}{24}\left(\frac{\alpha}{\bar{v}_z}\right)^2 a_0 - \frac{1}{24}\frac{\alpha b^2}{\bar{v}_z^3}a_0\right)$$

$$= -\frac{1}{60}\frac{\alpha^2 b}{\bar{v}_z^3}a_0 - \frac{1}{120}\frac{\alpha^2 b}{\bar{v}_z^3}a_0 - \frac{1}{120}\frac{\alpha b^3}{\bar{v}_z^4}a_0$$

$$= -\frac{1}{40}\frac{\alpha^2 b}{\bar{v}_z^3}a_0 - \frac{1}{120}\frac{\alpha b^3}{\bar{v}_z^4}a_0$$

$$a_6 = \frac{\alpha}{\bar{v}_z}\frac{3}{30}a_4 + \frac{b}{\bar{v}_z}\frac{1}{6}a_5$$

$$= \frac{\alpha}{\bar{v}_z}\frac{1}{10}\left(-\frac{1}{24}\left(\frac{\alpha}{\bar{v}_z}\right)^2 a_0 - \frac{1}{24}\frac{\alpha b^2}{\bar{v}_z^3}a_0\right) + \frac{b}{\bar{v}_z}\frac{1}{6}\left(-\frac{1}{40}\frac{\alpha^2 b}{\bar{v}_z^3}a_0 - \frac{1}{120}\frac{\alpha b^3}{\bar{v}_z^4}a_0\right)$$

$$= -\frac{1}{240}\left(\frac{\alpha}{\bar{v}_z}\right)^3 a_0 - \frac{1}{120}\left(\frac{\alpha b}{\bar{v}_z^2}\right)^2 a_0 - \frac{1}{720}\frac{\alpha b^4}{\bar{v}_z^5}a_0$$

$$\omega_{zz}(z) = a_0 - \frac{1}{2}\frac{\alpha}{\bar{v}_z}a_0 z^2 - \frac{1}{6}\frac{\alpha b}{\bar{v}_z^2}a_0 z^3 - \frac{1}{24}\left[\left(\frac{\alpha}{\bar{v}_z}\right)^2 + \frac{\alpha b^2}{\bar{v}_z^3}\right]a_0 z^4 - \left(\frac{1}{40}\frac{\alpha^2 b}{\bar{v}_z^3} + \frac{1}{120}\frac{\alpha b^3}{\bar{v}_z^4}\right)a_0 z^5$$

$$-\left[\frac{1}{240}\left(\frac{\alpha}{\bar{v}_z}\right)^3 + \frac{1}{120}\left(\frac{\alpha b}{\bar{v}_z^2}\right)^2 + \frac{1}{720}\frac{\alpha b^4}{\bar{v}_z^5}\right]a_0 z^6 + \cdots\cdots$$

From $\omega_{zz}(0) = \omega_{z\max}$, one gets:

$$a_0 = \omega_{zz\max} \tag{A4}$$

Taking the first three terms gives equation (19) with differences shown in Table 3.

Appendix 2. Theoretical model analysis

As $\omega_z(r,z)$ depends on attenuation of $\bar{v}_r$ and $\bar{v}_z$, variations of ω_z and V_θ along the z direction have to be studied. How accurate is the valuation velocity depends on V_z and V_θ, α and the slope of the line $\frac{\partial V_z}{\partial z}$, and the difference in Table 4 and Fig. 10 of α and b.

From equations (38) to (40) and Table 2, variation of $\frac{\omega_z}{\omega_{z\max}}$ and $\frac{V_\theta}{V_{\theta\max}}$ for flame swirling can be deduced. The radial variations of $\frac{\omega_z}{\omega_{z\max}}$ for the three pool fires at different heights are shown in Fig. 2A1(a) to (c). The value of $\frac{\omega_z}{\omega_{z\max}}$ at r = 0 is different, but $\frac{\omega_z}{\omega_{z\max}}$ is lower than 1 when the flame height is short. $\frac{\omega_z}{\omega_{z\max}}$ decreases as the distance away from flame axis increases, and the differences

of $\frac{\omega_z}{\omega_{z\max}}$ become smaller and approaches zero eventually. Upon generating a fire whirl, the flame radius r_m becomes smaller than the pool fire radius. The positions at which $\frac{\omega_z}{\omega_{z\max}}$ becomes 0 are 0.2 m, 0.26 m and 0.46 m for the fire pools SW-S, SW-M and SW-L respectively. From these values, it can be seen that in fire whirl, $\frac{\omega_z}{\omega_{z\max}}$ is reduced to zero at radial distance twice the vortex radius as shown in Fig. 2A1.

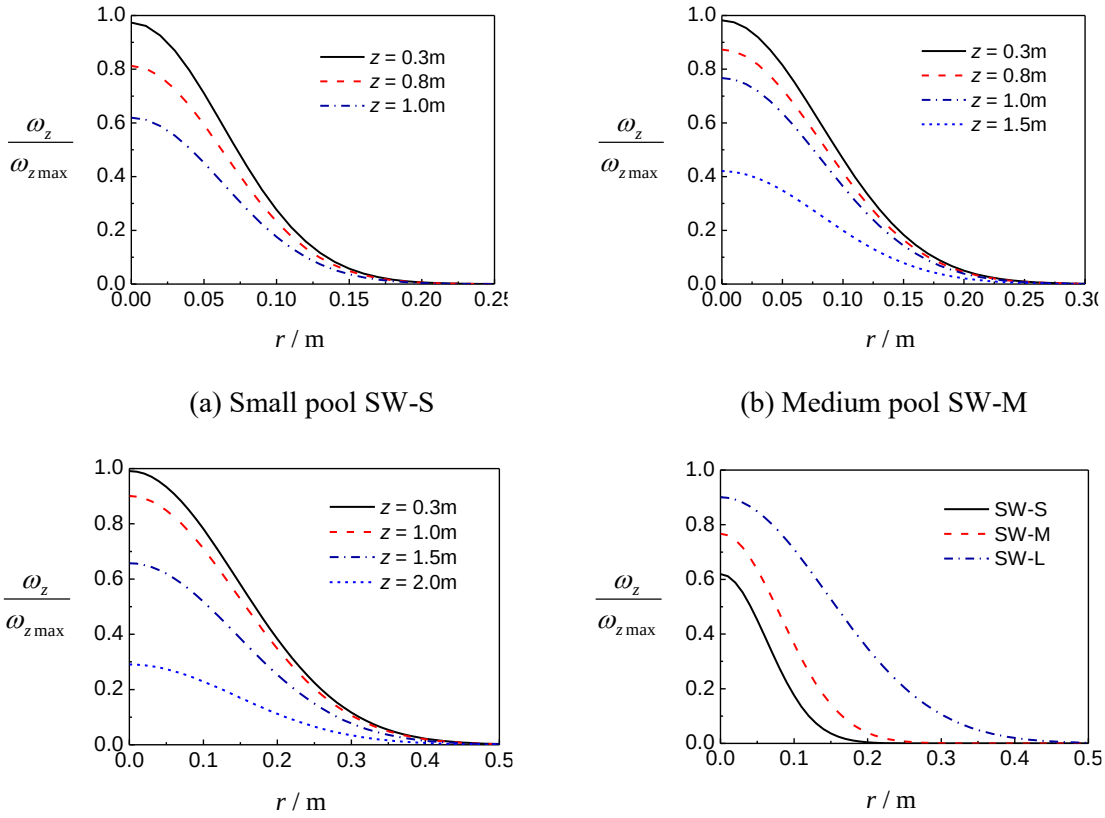

(a) Small pool SW-S

(b) Medium pool SW-M

(c) Large pool SW-L

(d) At 1 m above fire pool surface

Fig. 2A1: Radial variation of $\frac{\omega_z}{\omega_{z\max}}$ in a fire whirl

Radial variation of $\frac{\omega_z}{\omega_{z\max}}$ for the three experiments at 1 m height are shown in Fig. 2A1(d). The attenuation trends are similar but the value of $\frac{\omega_z}{\omega_{z\max}}$ at $r = 0$ is different. The value of $\frac{\omega_z}{\omega_{z\max}}$ at $r = 0$ is determined by the heat release rate of the pool fire. The flame height increases as the heat release rate increases. In equation (9), $\overline{V}_z$ is the momentum attenuation of ω_z along the z-direction .Smaller swirling flame height means less attenuation. Value of $\frac{\omega_z}{\omega_{z\max}}$ is near to 1. For larger pool fires, the

value of $\frac{\omega_z}{\omega_{z\max}}$ at $r = 0$ is larger.

The vertical variation of $\frac{V_\theta}{V_{\theta\max}}$ for the three experiments in fire whirl is shown in Fig. 2A2. The flame has the largest swirling velocity, giving a value $\frac{V_\theta}{V_{\theta\max}}$ of 1 at $z = 0$. When height increases, V_θ reduces, and thus $\frac{V_\theta}{V_{\theta\max}}$ also reduces. With different pool fire heat release rates and at different heights, the variations of $\frac{V_\theta}{V_{\theta\max}}$ are different. At 0.5 m, the small pool fire gives $\frac{V_\theta}{V_{\theta\max}}$ a value of 0.93, the medium pool fire 0.95, and the large pool fire 0.97. At 1 m, the values of $\frac{V_\theta}{V_{\theta\max}}$ for the small, medium and large pool fires are 0.66, 0.79 and 0.9 respectively, with a corresponding decrease of 34%, 21% and 10%, compared with the value at 0.5 m. Thus, a higher heat release rate would give a lower rate of attenuation of $\frac{V_\theta}{V_{\theta\max}}$.

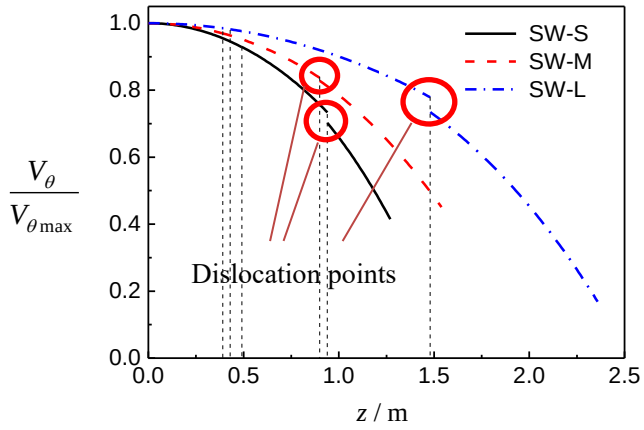

Fig. 2A2: Vertical variation of $\frac{V_\theta}{V_{\theta\max}}$ in a fire whirl

As shown in Fig. 2A2, there are two points of discontinuity on each line. The presence of discontinuity points arises from the artificial division of the flame region into the three sections.

V_z is taken to be the value along the central vertical axis (R=0). V_θ is the value along the z direction at R, now shown in Fig. 2A3.

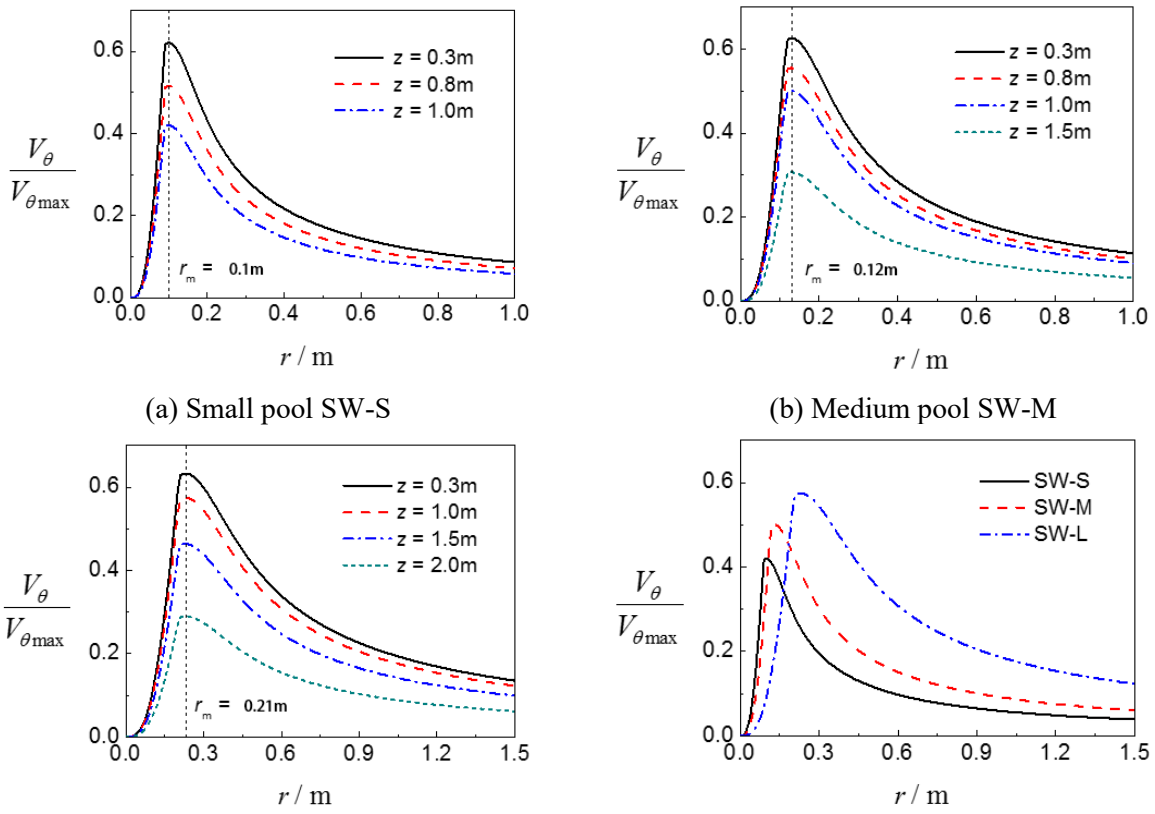

(a) Small pool SW-S

(b) Medium pool SW-M

(c) Large pool SW-L

(d) At 1 m above fire pool surface

Fig. 2A3: Radial variation of $\frac{V_\theta}{V_{\theta max}}$ in a fire whirl

The radial variation of $\frac{V_\theta}{V_{\theta max}}$ is shown in Fig. 2A3(a) to (c). The value of $\frac{V_\theta}{V_{\theta max}}$ is zero at the flame axis, and then increases with r at a rate of r^n (n >1) until a maximum is reached at the flame radius r_m. For $r > r_m$ $\frac{V_\theta}{V_{\theta max}}$ decreases. For the same fire, $\frac{V_\theta}{V_{\theta max}}$ decreases as height increases. This indicates that flame swirls more vigorously at lower levels.

The radial variation of $\frac{V_\theta}{V_{\theta max}}$ at 1 m is shown in Fig. 2A3(d) for different pool fires. It can be seen that a small pool fire (that is, low heat release rate) has small $\frac{V_\theta}{V_{\theta max}}$ at the same height. This further confirms that the heat release rate in a pool fire is a key factor in affecting flame swirling characteristics.